The Role of Moist Entropy on Termination of Madden-Julian Oscillation Events

By

Brett C. Chrisler

Submitted to the graduate degree program in Geography and Atmospheric Science and the Graduate Faculty of the University of Kansas in partial fulfillment of the requirements for the degree of Master of Sciences.

Chair: Justin P. Stachnik

David B. Mechem

David A. Rahn

Date Defended: 19 December 2019

The thesis committee for Brett C. Chrisler certifies that this is the approved version of the following thesis:

The Role of Moist Entropy on Termination of Madden-Julian Oscillation Events

Chair: Justin P. Stachnik

Date Approved: 19 December 2019

Abstract

The Madden-Julian oscillation (MJO) is the leading mode of intraseasonal variability in the tropics. Although many studies have examined the MJO, few have considered its termination. Multiple indices exist to track and forecast the MJO although the details of each index to MJO decay have not been documented. This study presents an intercomparison of several MJO indices for a 34-year period to examine the evolution of MJO events and comprise an index-specific climatology for MJO termination. We present an analysis of common indices including the OLR-based MJO Index (OMI) and filtered OMI (FMO) in addition to the Real-time Multivariate MJO (RMM) and velocity potential MJO (VPM) index.

Normalized EOF comparisons reveal only minor longitudinal and time shifts in the corresponding convection and circulation anomalies between indices. The absolute and fractional daily rate-of-change (ROC) of each index is derived and the RMM and VPM indices experience nearly twice the daily amplitude changes than the univariate indices. Results from the ROC analysis are implemented in an MJO event identification algorithm to study the sensitivity of MJO termination to changes in the temporary minimum amplitude and threshold used to define MJO events. The corresponding counts of primary, continuing, and circumnavigating events were recorded with primary events being insensitive to buffer changes, generally less than 5% among indices. Finally, an MJO climatology is created that presents MJO termination as a function of phase for each index.

Recent studies have also examined moist entropy (ME) as a proxy for moist static energy (MSE) and the relative role of the underlying processes responsible for changes in ME that potentially affect MJO propagation in GCMs. We present an analysis of the intraseasonally varying (ISV) ME throughout the lifetime of MJO events. A climatology of primary, continuing,

and terminating MJO events is created from the four indices used earlier. ME composites for all indices show a break in the wavenumber-1 oscillation at Day 0 for terminating events in nearly all domains except RMM Phase-6 and 7. Statistical significance between the mean ISV ME for continuing and terminating events is identified on average 10 days prior to MJO termination and 20 days prior in some cases.

ME tendency is decomposed into horizontal and vertical advection, sensible and latent heat fluxes, and vertically integrated shortwave and longwave heating using reanalysis. The relative role for eastward propagation of the MJO for each of these processes is calculated. For continuing events over the RMM Phase-2 domain, the total ME tendency is attributed mostly to horizontal ME advection although differences in the relative roles for vertical ME advection and radiative fluxes appear as early as 15 days prior to MJO termination. The analysis suggests processes other than horizontal advection may inhibit further eastward propagation and lead to MJO decay over this domain.

Acknowledgments

Special thanks to Michael Ventrice for providing the VPM EOFs and helpful discussions pertinent to the early part of this work. Also, special thanks to Xianan Jiang for helpful discussions related to this work and technical assistance with the moist entropy calculations. The RMM index was obtained from the Australian Bureau of Meteorology website. The OMI, FMO, and VPM data were provided by the NOAA/Office of Oceanic and Atmospheric Research (OAR)/Earth System Research Laboratory (ESRL) Physical Sciences Division (PSD) in Boulder, CO, USA, and obtained from their website at http://www.esrl.noaa.gov/psd/. ECMWF ERA-Interim data have been obtained from the ECMWF data server. This research was funded in part by a start-up grant from the College of Liberal Arts & Sciences at the University of Kansas.

A huge thank you to my advisor, Dr. Justin P. Stachnik, for all his support and countless hours assisting with research and my thesis. Much appreciation to my committee members Dr. David A. Rahn and Dr. David B. Mechem for all their feedback and insight that improved this body of work. Thank you to the Department of Geography and Atmospheric Science faculty and students for the opportunity to further my academic career and creating an enjoyable working environment. Thank you to Jordan Eissner, Luke McMichael, and Laura Tomkins for allowing me into their workspace to ask my pressing questions, for their constructive discussion, and to take a reprieve from my work. I am thankful for Elijah Barczewski for the positive reinforcement and helping with mental health. Thank you to all my friends and family who have supported me in all my endeavors. And most of all, thank you to my mother, who was a huge support system throughout my life; I would not be here without you and I miss you every day.

Table of Contents

List of Tables

List of Figures

Chapter I: Introduction

The Madden-Julian oscillation (MJO) is the leading mode of intraseasonal variability in the tropics. The MJO consists of a large-scale circulation that is often coupled with convection and canonically occurs in the Indian Ocean into the western Pacific (Madden and Julian 1971, 1972). This planetary scale phenomenon significantly affects the weather and climate of the Indian Ocean and the western Pacific and has far-reaching influences on the global scale. Variable rainfall is observed in association of the MJO in monsoon regions (e.g., Lau and Chan 1986; Matthews 2004; Wheeler and Hendon 2004; Lim et al. 2017). Additional global impacts include effects on the genesis of tropical cyclones in the Pacific Ocean and Caribbean (e.g., Hall et al. 2001), mid-latitude weather anomalie (e.g., Higgins et al. 2000, Bond and Vechhi 2003; Guan et al. 2012), and impacting the El Nino-Southern Oscillation (ENSO) (e.g., Lau and Waliser 2005). Although there are significant global effects associated with the MJO, there is no unified theory for its initiation, maintenance, and termination.

The MJO consists of cloudiness and deep convective anomalies that are associated with lower-level (upper-level) convergence (divergence) with a lifetime of 30-90 days (e.g., Zhang 2005). There are active and suppressed phases of the MJO in which the active phase results in higher rates of precipitation, cloudiness, and convection, while the suppressed phase has the opposite. It is important to note that there is still convection and precipitation that occurs during the suppressed phase, albeit to a lesser extent. The MJO tends to be stronger in boreal winter (November – April), but can occur throughout the year with latitudinal shifts following the location of the Intertropical Convergence zone and monsoon troughs (Zhang and Dong 2004). While convectively coupled, the overall eastward propagating MJO envelope contains westward propagating convection (e.g., Nakazawa 1988). The overall eastward propagation has been

attributed to eastward moving Kelvin waves and dry air being injected on the westward side of the MJO (Kerns and Chen 2014) although the exact reason for the eastward propagation and relatively slow propagation speed remains unknown.

The MJO most often initiates in the Indian Ocean, albeit only half of initiation events materialize in this region (e.g., Matthews 2008; Straub 2013; Stachnik et al. 2015a). The MJO propagates eastward at approximately 5 m s^{-1} (e.g., Zhang 2005). The MJO demonstrates multi-scale variability with circulation anomalies peaking at zonal wavenumber-1 and convection anomalies occurring more broadly across zonal wavenumbers 1-3 (Wheeler and Kiladis 1999). Eventually the MJO terminates and the convective anomalies decouple from the upper-level circulation. This process canonically occurs in the central and east Pacific although the upper-level circulation can be tracked around the globe as the dry disturbance propagates faster to the east (e.g., Madden and Julian 1994).

While MJO initiation has been studied thoroughly, less focus has been attributed to what conditions may lead to the termination of the MJO. Stachnik et al. (2015a) created a climatology of MJO events using spatial and temporal criteria that include initiation events that arise from a weak MJO signal (primary), those that have occurred from an already established, strong MJO signals (continuing), and events where propagation has ended and/or intraseasonal oscillation magnitude decayed (terminating). After observing differences between continuing and terminating events, they observed that the background lower-level (850-700 hPa) specific humidity associated with intraseasonal vertical circulation anomalies was a precursor condition for the eventual demise of the MJO in all regions. Additionally, the MJO may terminate over the Maritime Continent due to effects from friction and orography (e.g., Inness and Slingo 2007; Tseng et al. 2017), the diurnal cycle (e.g., Hagos et al. 2016), short-term dry signals eroding

moist anomalies (DeMott et al. 2018), and disruption of winds ahead of the MJO (Inness and Slingo 2007).

Since the MJO is convectively coupled, there are multiple indices that are used to track and forecast the MJO by using parameters that consider either/both the convective and the circulation components. The most popular of these indices is the Real-time Multivariate MJO (RMM) index (Wheeler and Hendon 2004), which uses zonal winds at 200 hPa and 850 hPa and outgoing longwave radiation (OLR). Another index that is entirely dynamically based is the velocity potential MJO (VPM) index (Ventrice et al. 2013), which uses zonal winds at 200 hPa and 850 hPa like the RMM index but includes velocity potential as a proxy for convection. Other common indices are based entirely on convection such as the OLR MJO Index (OMI) and Filtered OLR MJO index (FMO) as described by Kiladis et al. (2014). Analyzing these indices and their sensitivity when observing the maintenance and the termination of the MJO may shed light on the precursor conditions that help lead to the MJO continuing or terminating within a domain.

Global climate models (GCMs) struggle with simulating the eastward propagation of the MJO (e.g., Jiang et al. 2015). GCMs often employ a "moisture mode" framework of the MJO (Yu and Neelin 1994; Raymond and Fuchs 2009; Sobel and Maloney 2013), which views the MJO as a convectively-coupled disturbance where convection is regulated heavily by moisture anomalies. This framework has been studied using multiple variables including specific humidity (e.g., Maloney 2009), gross moist stability (e.g., Benedict et al. 2014), moist static energy (e.g., Wang et al. 2017), and moist entropy (e.g., Raymond 2009; Benedict et al. 2014). Models that have better agreement with observations include a more pronounced west-east gradient in moisture anomalies and tend to perform better for metrics evaluating the eastward propagation of

the MJO (Jiang 2017). Furthermore, the moist static energy can be decomposed into changes from advection, radiative, and surface flux components to view what physical processes that may assist in eastward propagation versus those that halt the propagation of the MJO (e.g., Jiang 2017).

Following the work of Stachnik et al. (2015a), we analyze four common indices that track and forecast the MJO to create a climatology of MJO events that continue through a phase domain or terminate. The sensitivity to index choice and their metrics is studied first as these results may inform algorithms used to identify MJO events before then studying the moist static energy budget terms associated with their decay. Results from each of these objective are presented in the following chapters with a brief summary of results in Chapter 4.

Chapter II: An Index Intercomparison for MJO Event Termination

2.1. Introduction

The Madden-Julian oscillation (MJO) is a large-scale phenomenon that generates intraseasonal convection and circulation anomalies in the tropics (Madden and Julian 1971, 1972). The MJO is the leading mode of intraseasonal climate variability and responsible for rainfall variability observed over the Pacific islands (Madden and Julian 1994) and monsoon regions of Asia (e.g., Lawrence and Webster 2002), Australia (e.g., Hendon and Liebmann 1990), North America (e.g., Bond and Vecchi 2003), South America (e.g., Liebmann et al. 2004), and Africa (e.g., Matthews 2004). The MJO has also been linked to tropical cyclones genesis, intensity, and tracks in the Pacific Ocean and Caribbean Sea (Maloney and Hartmann 2000; Hall et al. 2001; Jiang et al. 2012; Zhang 2013). In addition, the MJO has pronounced remote effects on surface winds in the equatorial Atlantic Ocean (Foltz and McPhaden 2004) and mid-latitude weather (e.g., Higgins et al. 2000; Bond and Vecchi 2003; Guan et al. 2012). On the largest scales, the MJO may impact the onset of El Niño-Southern Oscillation (ENSO) events (e.g., Lau and Waliser 2005), modify global momentum (Weickmann et al. 1997), and affect the Earth's electric and magnetic fields (Anyamba et al. 2000).

Initiation of the MJO most often occurs in the Indian Ocean with subsequent decay in the west Pacific. However, over half of initiation events occur in other regions (e.g., Matthews 2008; Straub 2013). The MJO generally propagates eastward at approximately 5 m s^{-1} as a broad envelope of convection and outgoing longwave radiation (OLR) anomalies with a typical oscillation period of 30 to 90 days (Zhang 2005). The MJO involves multi-scale variability of deep convection (Chen et al. 1996) where individual convective clusters move westward within

the overall eastward movement of the MJO (e.g., Nakazawa 1988). The westward movement of individual clusters is most likely due to westward propagating Rossby waves that occur within the MJO, which can also potentially alias and project upon common indices used to monitor and track the MJO (Roundy et al. 2009). The source of the large-scale, eastward propagation generally remains more elusive but is likely influenced by eastward propagating Kelvin waves and dry air funneling into the western side of the MJO by symmetric Rossby gyres (e.g., Kerns and Chen 2014). Zonal gradients in moist static energy (MSE), with higher values of MSE eastward and downstream of the active phase MJO, may also aid in the eastward propagation of convection over the Indo-Pacific region (Jiang 2017; Wang et al. 2017).

Other salient characteristics of the MJO can be scrutinized for its identification utilizing satellite observations, reanalyses, and/or global climate models (GCMs). For example, the zonal circulation of the MJO typically develops as a wavenumber-1 anomaly whereas there is a broader spectral peak ranging from zonal wavenumbers 1-3 for the anomalous convection (Zhang 2005). The seasonal cycle of the MJO has a peak in the austral summer and fall (i.e., November – April) associated with the Australian summer monsoon (e.g., Hendon and Liebmann 1990) and is concentrated between 5-10°S (Zhang and Dong 2004). A secondary maximum in MJO activity exists in the boreal summer with a spectral peak just north of the equator between 5-10°N (Zhang and Dong 2004). As the MJO propagates eastward over the Maritime Continent, the circulation features eventually decouple from the anomalous convection and the upper-level component of the zonal wind anomalies increases in propagation speed and may circumnavigate the globe. Consequently, most indices used to measure the MJO are global in nature and involve various combinations of metrics for convection and/or divergence (e.g., OLR, precipitation, brightness temperature, and upper-tropospheric velocity potential) or

circulation anomalies (e.g., 850 hPa and 200 hPa zonal wind). Additional techniques for monitoring the strength of the MJO involve simple analysis of variance, space-time filtering (e.g., Wheeler and Kiladis 1999), anomalous east-west power ratio (e.g., Waliser et al. 2009), and lag-regression (e.g., Jiang et al. 2015), among other process-oriented diagnostics to assess MJO fidelity in climate models (Kim et al. 2014).

Given the difficulty with modeling the MJO (e.g., Slingo et al. 1996, Waliser et al. 1999; Hung et al. 2013; Jiang et al. 2015), multiple studies have explored the potential physical causes that prevent GCMs from accurately simulating MJO initiation and eastward propagation (e.g., Bechtold et al. 2008; Hannah and Maloney 2011; Benedict et al. 2013; Klingaman and Woolnough 2014a; Klingaman and Woolnough 2014b). More recently, Wang et al. (2017) and Jiang (2017) noted an east-west contrast of MSE as critically important for the eastward propagation in GCMs. Gonzalez and Jiang (2017) further analyzed 23 simulations from the MJO Task Force simulations (Jiang et al. 2015) during boreal winter and found that eastward propagation was simulated poorly in models with reduced values of mean, low-level (i.e., 900-650 hPa) specific humidity over the Maritime Continent (MC).

Faced with the lack of a unified theory for MJO initiation, a significant body of research during the past decades has focused on MJO initiation in observations and models, including field campaigns that analyze the surrounding environmental signals and physical properties preceding an MJO (Yoneyama et al. 2013; Zhang et al. 2013). Studies of MJO initiation have examined the relative role of sea-surface temperatures (Wang and Xie 1997; Lau and Shen 1998), air-sea fluxes (Zhang and McPhaden 2000), moisture and convergence in the planetary boundary layer (Salby et al. 1994; Wang 1998), and cloud feedbacks involving shortwave and longwave radiation (Raymond 2001; Grabowski 2003). The MJO can also initiate due to forcing

from higher latitudes including Rossby wave propagation and baroclinic eddies (Zhao et al. 2013) or cold-air outbreaks from mid-latitudes over the tropics (Wang et al. 2012).

Whereas the previous studies (among others) have focused on developing theories and investigating potential mechanisms for initiating the MJO, this work focuses on a more novel topic: its termination and demise. Far fewer studies have explored potential MJO termination and decay mechanisms for observed events (e.g., Stachnik et al. 2015a; Demott et al. 2018), the weakening of intraseasonal anomalies in simple mathematical models (e.g., Stachnik et al. 2015b; Székely et al. 2016), and/or the failure to initiate (i.e., quiescent periods of the MJO). Stachnik et al. (2015a) produced a termination climatology for individual MJO events, although their analysis was limited to a single MJO index. Moreover, Stachnik et al. (2015a) identified differences in vertical advection as chiefly responsible for MJO decay, whereas studies since suggest horizontal advective processes are most important for event maintenance and continued eastward propagation of the MJO (e.g., Jiang 2017).

A next step towards resolving these differences and determining the physical mechanisms associated with weakening of the MJO is to build a termination climatology for multiple MJO tracking indices. The goal of the current study is to conduct an intercomparison of common MJO indices and document the sensitivity regarding MJO event termination. Such work is necessary in order to better inform future studies investigating precursor physical conditions for MJO termination and decay.

This article is organized as follows. Section 2 provides an overview of four popular MJO indices using empirical orthogonal functions (EOFs) of intraseasonally varying OLR, zonal wind, and/or velocity potential anomalies. We also review the MJO event identification algorithm originally described in Stachnik et al. (2015a). Correlations among the indices are

presented in Section 3, with a rate-of-change (ROC) analysis to examine average daily amplitude variations for each index. We also examine the history of MJO events for each index and the corresponding sensitivity of index-specific ROC parameters in the event identification algorithm. Section 3 fittingly ends with a climatology of MJO termination and Section 4 closes with a brief summary along with ongoing and future work related to MJO termination and decay.

2.2. Data and Methods

2.2.1. MJO Indices

The salient characteristics of the MJO include anomalies in low-level (upper-level) convergence (divergence) collocated with enhanced cloudiness and deep convection. Wavenumber-frequency filtering diagrams (e.g., Wheeler and Kiladis 1999) can identify spectral peaks in OLR, zonal winds, and/or precipitation in the space occupied by the MJO (i.e., eastward propagating, intraseasonal frequency, and low wavenumber). These techniques cannot be employed in real-time given the need for future data to identify intraseasonally filtered waves at the present. Other physical parameters have thus been explored for real-time monitoring and forecasting of the MJO. Common MJO indices retrieve the principal components when projecting daily raw or time-filtered data onto empirical orthogonal functions (EOF) representing the intraseasonally varying component of convection and circulation anomalies.

Univariate and multivariate indices exist that employ the above EOF analysis technique and are used extensively throughout the MJO literature. Popular multivariate indices include the Real-time Multivariate MJO (RMM) index (Wheeler and Hendon 2004), which uses both outgoing longwave radiation (OLR) from observations and 200 hPa and 850 hPa zonal winds from reanalysis data. The Velocity Potential MJO (VPM) index (Ventrice et al. 2013) is like the

RMM with the notable substitution of 200 hPa velocity potential in place of OLR. The VPM index thereby represents a purely dynamical representation of the MJO circulation anomalies using velocity potential (and corresponding divergence) as a proxy for convection. The RMM and VPM are equatorially averaged from 15°S to 15°N with the first four harmonics and time mean of the climatological cycle removed before calculating the annual average, zonal average EOFs. A 120-day running average is further subtracted from both indices to remove longer-term variability. Finally, the RMM index also removes any variability due to ENSO. This is not the case for the VPM index, although the effects of additional filtering are likely insignificant since Lin et al. (2008) found the 120-day interannual removal was sufficient at eliminating longer-term variability.

Univariate indices include the OLR MJO Index (OMI) and the Filtered OLR MJO (FMO) Index. Unlike the RMM and VPM, the OMI projects 20-96 day filtered OLR anomalies onto *daily* EOFs of 30-96 eastward filtered OLR that vary in latitude (i.e., no zonal averaging). Additional details for the OMI are provided in Kiladis et al. (2014). The FMO also uses 20-96 daily filtered OLR but projects this data onto a yearly EOF pattern, which is equatorially averaged between 15°S to 15°N. The present study uses a 34-year climatology (April 1979 – February 2013) with overlapping availability for all indices, along with subsets from the Year of Tropical Convection (YOTC) from May 2008 – April 2010 (Waliser and Moncrieff 2008) and Dynamics of the Madden-Julian Oscillation (DYNAMO) field campaign from October 2011 – March 2012 (Yoneyama et al. 2013), to conduct an intercomparison between indices.

Each of the MJO indices in this study calculates the first two leading EOFs for the meteorological parameters specific to that index. The percent variance for the first two EOFs ranges from 25% for the RMM (Wheeler and Hendon 2004) to a maximum of 65% using the

OMI (Kiladis et al.; 2014). Because the OMI data uses spatially varying, daily EOFs, we first calculate a corresponding zonal average of the two-dimensional EOF structures and then take a zonal average to arrive at an EOF structure directly comparable to the RMM, VPM, and FMO indices. We also perform a normalization to account for EOF magnitude variations among indices by removing the mean and dividing by the respective standard deviation for each index. A normalized value of 1.0 thus corresponds to a single standard deviation for the given EOF. Finally, the EOF order was interchanged and sign reversed for the OMI and FMO as necessary so the resulting EOF structures would better align with the RMM (e.g., -OMI EOF2 corresponds to +RMM EOF1 in the original data).

Figs. 2.1a and 2.1b show the first two leading EOFs of OLR for the RMM, OMI, and FMO. The corresponding 200 hPa velocity potential (a proxy for divergence and thus convection) from the VPM is plotted in Fig. 2.1c. For the structures best matching RMM EOF1 (Fig. 2.1a), there is a broad region of negative OLR anomalies from 100-150°E. A positive projection onto this structure thus implies active phase convective anomalies over the Maritime Continent and a broad region of suppressed convection across the western hemisphere and Africa. The shapes and magnitudes of all three EOFs are remarkably similar within Fig. 2.1a, although we note the peak in convection for the OMI occurs approximately 25°E of the corresponding OLR minima for RMM and VPM. This distance corresponds to a time lag of ~6 days assuming the MJO propagates at ~5 m s^{-1}. The OLR patterns are even better aligned for those EOFs matching RMM OLR EOF2, with the RMM, OMI, and FMO all having their highest and lowest values at approximately the same longitudes (Fig.2.1b). Here, the minimum in OLR occurs near 150°E for all three indices, which can be interpreted as the MJO convection having propagated eastward into the west Pacific. Peak positive EOF values are identified from 60-

100°E and indicate suppressed conditions over the Indian Ocean. The leading two EOFs are in quadrature for all indices (cf. Figs 2.1a and 2.1b).

The leading two EOFs for the 200 hPa velocity potential generally match the OLR EOFs for the RMM index (Fig. 2.1c). The velocity potential EOFs contain a wavenumber-1 structure that is smoother and slightly broader than the corresponding OLR EOFs. Nonetheless, peak amplitudes for the velocity potential EOF1 occur at the same longitudes as the RMM OLR EOF1. The VPM EOF2 has the same positive peak over the Indian Ocean with a much wider negative peak from 160°E-120°W, which occurs to the east of RMM OLR EOF2.

The analogous EOFs for zonal circulation anomalies are shown in Fig. 2.2. Only the multivariate indices (i.e., RMM and VPM) are plotted as they use relative zonal winds to identify the MJO in addition to OLR. As with the RMM EOFs described in Wheeler and Hendon (2004), the 850 hPa VPM winds shift from positive (westerly) to negative (easterly) near 135°E and imply low-level convergence for EOF1 (Fig. 2.2a). The 200 hPa winds are opposite the low-level pattern with upper-level divergence for the VPM EOF at the same location as the low-level convergence. Given the correspondence with the negative OLR anomalies in the region, both the RMM and VPM identify the MJO as a convectively-coupled circulation anomaly. The longitude where the VPM EOF1 winds switch from positive to negative values at 850 hPa (and vice versa at 200 hPa) is less than 10° west of the equivalent longitudes for the RMM EOFs. There is less agreement on the magnitude of RMM and VPM EOF2 (Fig. 2.2b) although the locations of the maximum westerly and easterly wind anomalies agree for both indices.

2.2.2. MJO Event Identification Algorithm

An event identification algorithm is implemented to define MJO events following

Stachnik et al. (2015a). This algorithm requires a sequence of days to be above some combined amplitude threshold (often unity, or one standard deviation) rather than simply examining dates with strong or weak MJO activity based on the index values without regard to temporal continuity. The algorithm is used to calculate totals of primary, continuing, and circumnavigating events, and an ensuing termination climatology specific to each index. Primary events are preceded by quiescent periods that arise from a weak MJO signal indicated with combined amplitude less than a given threshold (i.e., inside the unit circle) using the MJO phase-space diagram popularized by Wheeler and Hendon (2004) as illustrated in Fig. 2.3. To be considered a full-fledged MJO "event", the time-series must demonstrate eastward propagation through a minimum of four phases on the phase-space diagram while maintaining a combined amplitude greater than the threshold value. Transient weakening of the MJO below the event threshold is permitted by the algorithm pending that the combined amplitude always remains above some critical value and escapes the buffer zone within 3 days of the first occurrence of a weakened MJO. Stachnik et al. (2015a) used a threshold of 1.0, which corresponds to one standard deviation of intraseasonal anomalies, and a relatively small buffer of 0.1 for MJO events using the RMM index.

The default parameters from Stachnik et al. (2015a) are plotted in Fig. 2.3 and example classifications from the observed RMM dataset are shown in Fig. 2.4. The large gray marker denotes a primary (i.e., initiation) MJO event in Fig. 2.4a. This occurs when the index amplitude first exceeds the threshold in the RMM Phase-7 (Western Pacific) domain. A counter-clockwise trajectory on the phase-space diagrams indicates eastward propagation and the MJO is considered a continuing event (i.e., arising from an already established MJO) once accumulating two phases, provided it also continue another four phases to be considered its own event. In the

first example, the initial continuing event occurs once entering the RMM Phase-1 domain in Fig 2.4a. Additional continuing events occur in phase-2 and phase-3. Circumnavigating events are a special case of long continuing events that cycle through all eight phases and are followed by at least an additional four (e.g., RMM Phase-2 in Fig. 2.4b).

Fig. 2.4 also demonstrates the relative tolerance of the identification algorithm to stop premature termination of an MJO event. The combined amplitude briefly drops below the unity threshold when passing through phase-4 (i.e., Maritime Continent) in Fig.2.4a but remains above the critical value determined by the buffer of 0.1. Other instances of permitted transient weakening are also identified in phase-5, phase-2, and phase-3 in Figure 4b. The MJO is also allowed to retrograde by one phase (e.g., the westward propagation from RMM Phase-7 to RMM Phase-6 in Fig. 2.4b) so long as it eventually resumes accumulating phase and propagates to the east. Finally, a termination event may be caused by the index amplitude falling below the buffer, spending four days or more below the threshold but above the buffer, or if the MJO phase continuously retrogrades by more than one phase (i.e., clockwise rotation in the MJO phase-space diagram). Weak amplitude termination cases are shown in both Figs. 2.4a and 2.4b with the red marker.

Matthews (2008) compared primary and “successive” events, which are consistent with the terms primary and continuing used herein, using a different univariate index based only on OLR to observe the convective signal of the MJO. Matthews (2008) also constructed precursor environmental signals associated with initiating convective anomalies that included thermodynamic forcing, boundary-layer convergence and moisture, and forcing by the ocean and synoptic wave activity. Successive events and mature primary events contained positive anomalies of boundary-layer convergence and moisture, sea surface temperature (SST), and

synoptic wave activity, but these conditions did not necessarily precede a primary event. Suppressed convection anomalies were found to precede primary MJO events along with a growing negative (i.e., cold) mid-tropospheric temperature anomaly, which allowed the atmosphere to destabilize.

Stachnik et al. (2015a) quantified the frequency of MJO termination events, which peaked in phase-8 (Western Hemisphere) and phase-6 (Western Pacific) with 20.1% and 16.9% of all events, respectively. They further observed a link between terminating MJOs, lower-tropospheric mean-state moisture, and vertical circulation anomalies associated with intraseasonal variability when analyzing termination events identified by the RMM index. Given that different MJO indices rely on different meteorological parameters and often provide discrepant results of MJO amplitude and/or phase (e.g., Straub 2013), it remains possible that the results of Stachnik et al. (2015a) could be index specific. Comparing results from different indices could indicate if the RMM or particular event identification algorithm parameters are too limited, in addition to determining if a termination climatology is universal or sensitive to the choice of index. Any agreement or disagreement among indices may provide insight as to what parameters may lead towards termination and shutdown of the MJO.

2.3. Results

2.3.1. Time Series Analysis

A time-series analysis is first performed to document the similarity among the MJO indices. The Pearson correlation is calculated to determine which indices are most alike regarding both MJO amplitude and phase. An example from the DYNAMO period is shown in Fig. 2.5 where a simple visual analysis suggests a strong amplitude correlation between the

univariate (OMI and FMO) and multivariate (RMM and VPM) indices (Fig. 2.5a). Persistent phase accumulation is evident in the first part of the DYNAMO campaign for all indices. The RMM and VPM demonstrate marked westward propagation during January 2012 (Fig. 2.5b), which was generally characterized by a weak amplitude (i.e., less than 1.0) MJO for these indices during that time. The correlation coefficients for DYNAMO, YOTC, and the entire climatology are summarized in Table 2.1. All the correlation coefficients in Table 2.1 were determined to be statistically significant (i.e., *p*-values less than 0.01) from a 2-tailed test assuming normal distributions (see Section 2.3.2), although it should be noted that the indices are not truly independent given that they rely on common inputs and/or similar processing techniques.

Overall, the indices correlate well if both are either univariate or multivariate. For MJO amplitude, the OMI and FMO have correlation coefficients greater than 0.82 for all three periods (Table 2.1). The highest overall correlations were observed during the DYNAMO period for RMM and VPM (red and orange lines in Fig. 2.5, respectively) with a value of 0.93 (Table 2.1). For MJO phase, the OMI and FMO again display the highest correlations with values upwards of 0.80 during DYNAMO although a weaker R-value of 0.66 for the climatological period. The MJO phase during DYNAMO contained correlations ~0.40 for the VPM/OMI and VPM/FMO with higher values of ~0.70 for other dissimilar indices (i.e., RMM/OMI and RMM/FMO). These DYNAMO phase correlation coefficients were higher than the corresponding amplitude correlations between combinations of the univariate and multivariate indices (Table 2.1).

To determine if zonal shifts in the EOF peaks bias our correlations (e.g., Fig. 2.1a) we calculate the correlation R-values between the various indices at lags of +/- 30 days. The number of days offset with the greatest correlation coefficients is summarized in Table 2.1. There is a

maximum lag of 3 days between VPM/OMI in addition to VPM/FMO for both DYNAMO and YOTC. There is also a 3-day lag between RMM and OMI during DYNAMO. This represents half of the ~6 day lag (25° longitude) for RMM and OMI EOF1, assuming the MJO propagates at 5 m s^{-1}. Because the EOF structures have peaks at the same longitude for EOF2, we expect a maximum correlation of half the lag time for EOF1, which is consistent with our results. In contrast, there is a 0 day lag for OMI/FMO and RMM/VPM during the climatology and both periods (Table 2.1). The previous result again confirms that time-series of indices that are fundamentally alike contain a similar history and evolution of MJO events.

2.3.2. Rate of Change Analysis

Before constructing a termination climatology, it becomes worthwhile to know if parameters in the event identification algorithm need to be tuned for individual MJO indices. A rate-of-change (ROC) analysis was conducted and probability density functions (PDFs) were created to observe which indices have the greatest average daily change in combined amplitude. Skewness values of the PDFs were also calculated in order to reveal any tendencies towards negative or positive ROCs.

The resultant PDFs for all indices during the 34-year climatology are shown in Fig. 2.6. The skewness values are 0.023 (RMM), 0.131 (VPM), -0.009 (FMO), and -0.002 (OMI), where positive skewness corresponds to a longer tail on the increasing side and negative values the opposite. Nonetheless, all the skewness values are significantly less than twice the standard error, which indicates the dataset is normal and not skewed.

Most of the ROC values are centered on zero as the mean for all indices is approximately zero. The mean standard deviations of the ROC increase from 0.108 (OMI), 0.132 (FMO), 0.195

(RMM), and peak at 0.214 (VPM). Assuming a normal distribution, these numbers suggest that the average ROC for MJO amplitude may vary significantly more than the original 0.1 buffer magnitude applied in the event identification algorithm from Stachnik et al. (2015a). The original 0.1 amplitude buffer may have been too restrictive for counting MJO events, where events would terminate more quickly when experiencing larger daily ROCs. This would have larger implications on multivariate indices that have standard deviation values of approximately 0.2 compared to the univariate indices that were around the original tenth.

A valid question is whether there is any appreciable sensitivity of the ROC to the mean MJO index amplitude. To address this concern, the mean standard deviation of absolute ROC is calculated and binned by every tenth value of mean amplitude (Fig. 2.7). The results indicate an insensitive distribution that is about the same value as the overall standard deviations calculated from the initial probability density function. More simply, there is an equivalent value of ROC susceptibility regardless of mean amplitude. Fig 2.7 shows some spread for mean amplitudes greater than 3.5 (i.e., 3.5 standard deviations) although these sensitivities are likely due to a low sample bias (mean amplitudes with lower than 0.1% of total sample days are indicated with open circles).

To better account for the relative change between any bins, the mean standard deviation of fractional (i.e., daily ROC divided by the initial amplitude) rate-of-change is also calculated (Fig. 2.8). Mean value amplitudes between 0 and 0.1 are more susceptible to larger rates of fractional change with average standard deviation values greater than 2 given the small denominator and are plotted separately using their own scale. There is a decreasing trend as mean amplitude increases, which indicates less susceptibility to relative amplitude changes when the MJO is already well-established (i.e., high amplitude intraseasonal oscillations).

2.3.3. MJO Event Analysis

Counts of primary, continuing, and circumnavigating events are obtained from the event identification algorithm using both the original 0.1 buffer (Table 2.2) and an index-specific value from the previous ROC analysis (Table 2.3). We also explore the sensitivity of the threshold used to define MJO events with the amplitude increasing every tenth between 0.7 and 1.5 and a special high-amplitude case of 2.0. Increasing the threshold value has the trivial effect of decreasing the number of discrete time-series that qualify as MJO events for all indices regardless of the buffer strength. This includes up to a 90% reduction for primary MJO events with the VPM index, which decreases from 205 to 20 events using the weak (0.7) and strong (2.0) amplitude thresholds to define an event (Table 2.2). There is also a reduction of continuing and circumnavigating events as the threshold increases. Finally, we identify a consistent decrease in the number of days above the threshold and similar reduction in the average length of events. For the previous VPM case, the MJO event length decreases from 39.6 d to 18.7 d for the weak and strong amplitude thresholds, respectively (Table 2.2). Similar results are identified when increasing the threshold value for MJO events using the index-specific standard deviation buffer (Table 2.3).

A more meaningful comparison involves the number of MJO events for a given threshold when using the original tenth buffer and the index-specific values from the ROC analysis. Primary events have less than a ±5% change when investigating a given threshold for the original (0.1) or standard deviation buffer across the entire range of thresholds (cf. Tables 2.2 and 2.3). The change in MJO events is negligible for the OMI and FMO, which had average standard deviations of 0.108 and 0.132, respectively. Even the VPM, with an increase buffer strength from 0.10 to 0.214, demonstrated little change in the number of primary MJO events.

We thus conclude the number of primary (and thus terminal) MJO events is insensitive to the buffer magnitude for all four indices appearing in this study.

While the changes are small, the number of primary events can either increase or decrease as a result of increasing the buffer strength. Positive changes indicate more unique instances are qualifying as MJO events with the larger buffer. The number of MJO events could be reduced if two primary events that previously had values fall below the original tenth buffer no longer terminate with the new (larger) buffer and therefore become a single event.

Unlike with primary events, continuing and circumnavigating events have only zero or positive (i.e., non-negative) changes as a result of increasing the buffer from the original tenth to the mean standard deviation from the ROC analysis. The positive change for both continuing and circumnavigating events indicates that potentially more primary events are occurring that continue to propagate beyond four phases and create extra continuing events. In addition, the fusion of two primary events that become stitched together with the relaxed buffer magnitude thereby contribute positive changes to the continuing events. With higher amounts of continuing and circumnavigating events, there is also a corresponding increase in the average event length (cf. Tables 2.2 and 2.3). The largest increase was found in the multivariate indices, which again have the highest standard deviation buffers of all four indices. Using the unity threshold, the average event length increased by 1.0 days for the RMM and 1.9 days for the VPM index (Table 2.3). The average event length for the FMO only increased by 0.1 days and OMI remained constant for the unity threshold.

Curiously, the index intercomparison revealed that univariate OLR indices have longer event lengths than multivariate indices. For instance, the average event length decreases from 44.9 days (OMI) and 40.8 days (FMO) to 35.6 days (RMM) and 33.0 days (VPM) for the 1.0

amplitude threshold and standard deviation buffer case (Table 2.3). This is unexpected and counterintuitive as the circulation component of the MJO is typically observed well after convection has already waned. More research into this result is warranted but beyond the scope of our current study.

2.3.4. Termination Climatology

Radial-frequency plots in the Wheeler and Hendon (2004) phase-space domain are constructed that display the locations (phases) in which primary, continuing, and terminating events occur. We ignore the frequency of occurrence for circumnavigating events since they are relatively rare. The threshold amplitude is set at 1.0 with the standard deviation buffer used for all indices (Fig. 2.9).

Primary events have a maximum in phase-2 for the FMO and RMM with 21.1% and 18.1% of all initiation events, respectively (Figs. 2.9a and 2.9c). Initiation of primary events also peaks in phase-2 for VPM with 17.4% (Fig. 2.9b), and phase-5 for OMI with 18.5% (Fig. 2.8d). This result is expected as primary events often occur in phases 1-3 (Matthews 2008; Stachnik et al. 2015a). Maxima in continuing events are observed in phase-4 with values of 16.7% (FMO) and 15.8% (VPM) and in phase-5 with values of 16.4% (OMI) and 15.4% (RMM). Regardless of local maxima, the continuing event distribution is rather symmetric for all indices indicating a small change in percentage among phases. This result is also consistent with Stachnik et al. (2015a) where there is a roughly concentric curve for continuing events with only a small peak over the Maritime Continent.

Among all indices, phase-8 (Western Hemisphere) has the highest termination events with 29.4% (OMI), 23.1% (RMM), 21.1% (FMO), and 19.8% (VPM). Secondary termination

peaks occur in phase-1 (Africa) for all indices except RMM (17.9%, 15.1%, and 14.5% for the FMO, OMI, and VPM, respectively). RMM has a second maximum in phase-6 (Western Pacific) with 15.6% of all termination events. The RMM maximums are consistent with Stachnik et al. (2015a), and the ensemble of MJO indices agree that the plurality of termination events occur in the Western Hemisphere.

2.4. Summary and Discussion

Since only a few studies examine termination of the Madden-Julian oscillation (e.g., Stachnik et al. 2015a; Stachnik et al. 2015b; Székely et al. 2016; Demott et al. 2018] an intercomparison of indices was deemed necessary as a basis for future studies examining the physical precursors for MJO decay. An empirical orthogonal function intercomparison, time series correlations, and rate-of-change (ROC) analysis were performed. The average standard deviation of daily ROC was determined to provide index-specific statistical information that was implemented into an event identification algorithm following Stachnik et al. (2015a) and counts primary, continuing, circumnavigating, and terminating events by location and/or phase. Previous studies used unity as a threshold for an active MJO event with a tenth buffer to account for temporary fluctuations in MJO strength. This buffer was determined to be too conservative when calculating the standard deviation of rates-of-change for all the indices presented within this study, particularly for the multivariate RMM and VPM indices. These indices experienced nearly twice the daily amplitude change relative to the univariate OMI and FMO indices. Future work may explore potential changes to the event climatology when using phase-specific ROCs as it remains possible that the relative criteria for transient intensification, weakening, and/or termination may be a function of phase.

A termination climatology identifies that RMM Phase-8 (western hemisphere) contains the maximum for MJO termination events: 29.4% (OMI), 23.1% (RMM), 21.1% (FMO), and 19.8% (VPM). A second local maximum is found over phase-1 (Africa) in three indices: 17.9% (FMO), 15.1% (OMI), and 14.5% (VPM) and in phase-6 (Western Pacific) that accounts for 15.6% of RMM events. In addition, primary events maximized in phase-2 and phase-3 (Indian Ocean) for all indices except the OMI. The previous result is expected as the MJO is thought to commonly originate in the Indian Ocean though our results reinforce the notion from Matthews (2008) that more than half of all MJO events initiate outside of this domain. There was relatively good agreement regarding the phase of MJO termination events among all indices with the only outlier being the secondary maximum for the RMM. This consensus follows the long-established qualitative behavior of the MJO as indicated in Madden and Julian (1972) where the convective anomalies significantly weaken around the dateline in the Central Pacific and decouple with the corresponding anomalous circulation.

Multivariate indices may be a better proxy for MJO termination for a few reasons. There seems to be an extreme maximum in the OMI for terminating events comparative to the other indices. Moreover, the OMI and FMO have a larger discrepancy among continuing (e.g., 420 in OMI and 257 in FMO) and circumnavigating events (e.g., 30 in OMI and 16 in FMO) for the 1.0 amplitude threshold, while the VPM and RMM are closer in the total number of events (Table 2.3).

The RMM secondary termination maximum over phase-6 is consistent with studies regarding the interaction of the MJO with the Maritime Continent since weakening of the MJO here can cause event termination over this domain. Inness and Slingo (2007) analyzed the

orography of the MC and discovered that there is a significant disruption of winds and low-level pressure to the east of the propagating convection. Demott et al. (2018) also indicated there are transient dry precursor signals over the MC that weaken eastward moving moist anomalies, potentially leading to event termination.

Future work will consider the role of moist and dry static energy upon the decay and evolution of MJO termination events. Moist static energy (S) is calculated by letting the total water vapor condense and release latent heat under adiabatic conditions in addition to contributions from the dry static energy (i.e., sum of enthalpy and potential energy). The MSE is given by the following:

$$S = C_p T + gz + L_v r \qquad (1)$$

where C_p is the specific heat at constant pressure for dry air, T is absolute temperature, g is gravitational acceleration, z is height above some reference level, L_v is the latent heat of vaporization, and r is the water vapor mixing ratio. Recent studies examining MSE budgets (e.g., Jiang 2017; Wang et al. 2017; Gonzalez and Jiang 2017; Adames et al. 2017) and the MJO show promise for explaining the eastward propagation of the MJO in GCMs. Those GCMs that are deemed to be "good" models for eastward propagation contain more realistic free-tropospheric moisture patterns and east-west dipoles in MSE tendency ahead of the active MJO convection. While MSE has generally been applied to eastward propagation in GCMs, we intend to investigate MSE regarding observed MJO termination events. Furthermore, Matthews (2000) found that dry Kelvin waves from previous MJO activity cause mean sea-level pressure anomalies, which could assist in continuing events. Future work will also consider other physical precursor conditions associated with termination such as the interaction of other tropical wave modes with the MJO.

Table 2.1. Pearson correlation R-values for MJO amplitude and phase, as well lag in days for select periods.

	Period		
Indices	Climatology	YOTC	DYNAMO
	Pearson Correlation R-Values – Amplitude		
RMM/VPM	0.76	0.66	0.93
RMM/OMI	0.53	0.46	0.35
RMM/FMO	0.47	0.37	0.36
VPM/OMI	0.41	0.44	0.30
VPM/FMO	0.33	0.38	0.27
OMI/FMO	0.86	0.82	0.83
	Pearson Correlation R-Values - Phase		
RMM/VPM	0.49	0.43	0.53
RMM/OMI	0.43	0.33	0.70
RMM/FMO	0.41	0.39	0.71
VPM/OMI	0.35	0.21	0.39
VPM/FMO	0.29	0.22	0.40
OMI/FMO	0.66	0.68	0.80
		Lag (d)	
RMM/VPM	0	0	0
RMM/OMI	1	1	3
RMM/FMO	2	2	2
VPM/OMI	0	3	3
VPM/FMO	2	3	3
OMI/FMO	0	0	0

Table 2.2.. Counts of primary, continuing, and circumnavigating events by threshold using an amplitude buffer of 0.1 in the event identification algorithm, as well as length of event in days.

	Threshold									
Indices	0.7	0.8	0.9	1.0	1.1	1.2	1.3	1.4	1.5	2.0
					Primary					
RMM	192	181	167	156	153	125	106	96	81	23
VPM	205	189	181	169	150	135	119	96	79	20
OMI	142	131	127	119	113	103	90	78	66	26
FMO	134	122	105	94	83	69	62	50	41	20
					Continuing					
RMM	624	504	402	322	221	175	138	104	89	14
VPM	575	475	359	284	223	161	120	83	57	4
OMI	766	628	502	420	339	279	223	181	135	38
FMO	504	414	333	253	195	159	124	96	79	10
					Circumnavigating					
RMM	42	33	22	15	8	6	5	4	4	1
VPM	34	27	24	15	10	4	2	2	1	1
OMI	55	46	34	30	20	14	11	8	6	1
FMO	35	29	23	15	11	7	6	4	2	1
					Average Length of Events (d)					
RMM	41.4	39.2	37.2	34.6	30.0	30.3	29.3	27.5	27.1	23.6
VPM	39.6	37.6	33.4	31.1	29.9	27.8	25.5	24.8	23.9	18.7
OMI	56.4	52.6	47.5	44.9	41.3	29.5	37.6	36.7	34.4	32.2
FMO	48.1	45.8	43.9	40.9	37.8	36.8	34.9	34.8	34.9	26.7

Table 2.3. Same as Table 2.2, but using standard deviation as an amplitude buffer in the event identification algorithm.

	Threshold									
Indices	0.7	0.8	0.9	1.0	1.1	1.2	1.3	1.4	1.5	2.0
					Primary					
RMM	190	184	166	160	151	142	111	96	88	24
VPM	194	197	180	172	154	137	124	103	84	21
OMI	142	131	127	119	113	103	90	78	66	26
FMO	134	122	108	95	84	70	63	49	42	20
					Continuing					
RMM	702	570	464	357	280	191	157	125	94	17
VPM	673	535	448	335	259	202	138	105	73	10
OMI	766	630	506	420	343	279	226	181	135	38
FMO	523	430	335	257	199	159	132	103	82	11
					Circumnavigating					
RMM	48	39	30	17	12	7	6	5	4	1
VPM	41	33	26	19	14	9	4	2	2	1
OMI	55	46	34	30	21	14	11	8	6	1
FMO	37	30	24	16	12	7	6	5	3	1
					Average Length of Events (d)					
RMM	44.3	40.9	39.4	35.6	32.8	29.5	30.0	29.1	26.9	25.2
VPM	43.7	38.9	37.5	33.0	31.2	29.8	26.5	25.6	24.8	20.4
OMI	56.4	52.7	47.7	44.9	41.4	38.5	37.8	36.7	34.4	32.2
FMO	48.7	46.4	43.5	40.8	38.0	36.6	35.6	35.8	34.9	27.5

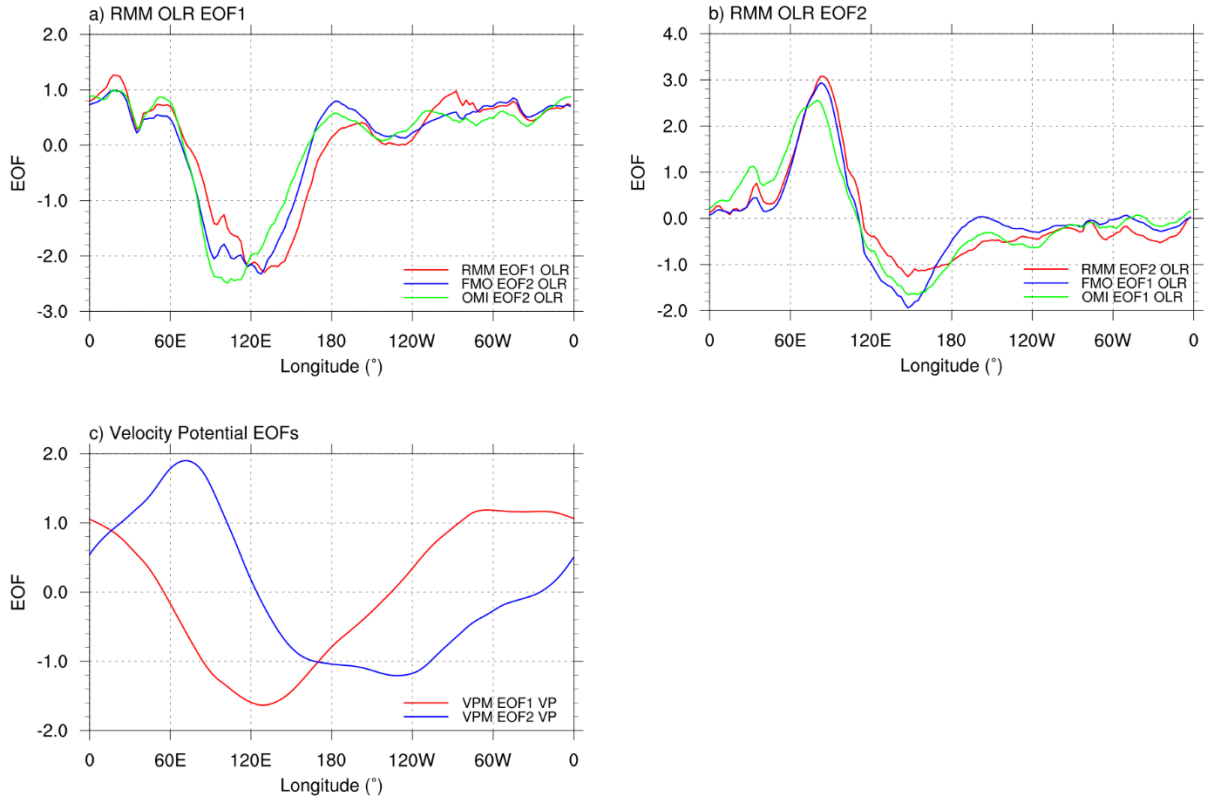

FIG 2.1. Normalized outgoing longwave radiation a) EOF1 and b) EOF2 patterns for the RMM index (red) with the corresponding EOF structures from the OMI (green) and FMO (blue). c) Normalized EOF1 and EOF2 of velocity potential for the VPM index. The sign and order of the OMI, FMO, and VPM EOFs was modified as necessary to match the RMM EOFs (see text).

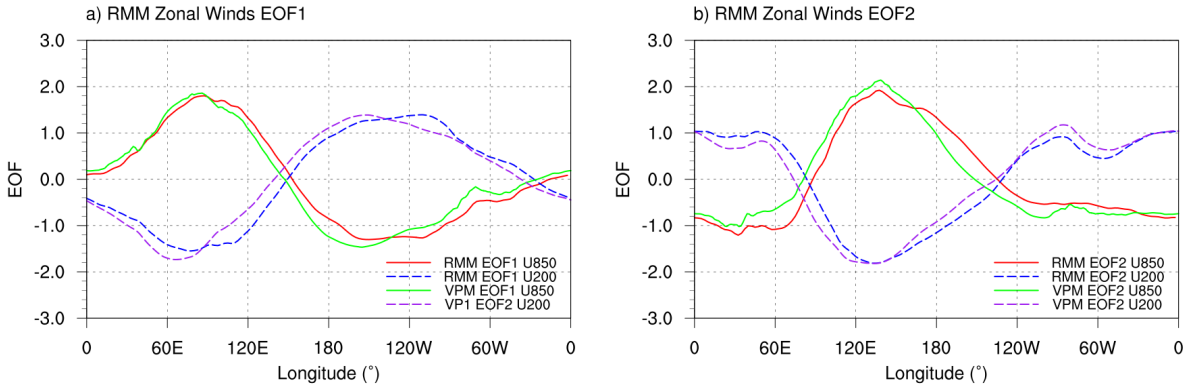

FIG 2.2. Normalized zonal wind a) EOF1 and b) EOF2 patterns for the RMM and VPM indices. Lower- (U850) and upper-level (U200) winds are shown in solid and dashed profiles, respectively. The sign and order of the VPM EOFs was modified as necessary to match the RMM EOFs (see text).

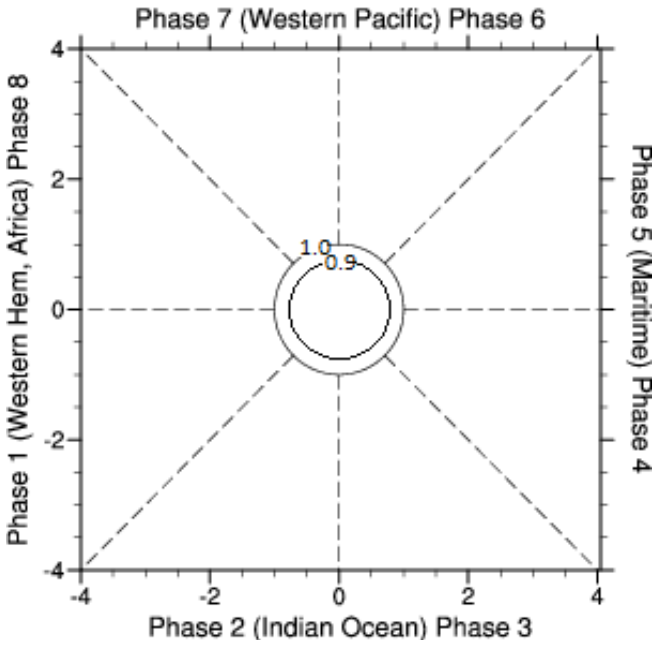

FIG 2.3. Example of MJO event identification algorithm threshold and buffer, where the combined amplitude may temporarily drop below the threshold (1.0) without experiencing immediate termination. An MJO event will not terminate provided it remain above the buffer (0.9) for no more than three consecutive days before again exceeding the threshold strength.

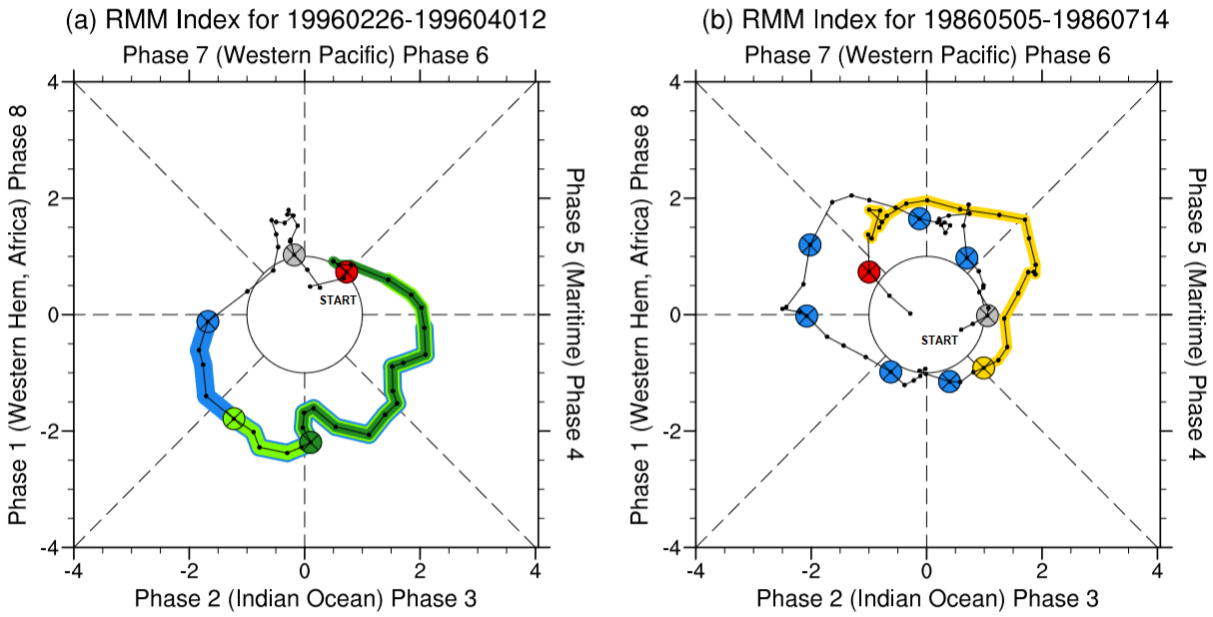

FIG 2.4. (a) 26 February 1996 – 12 April 1996 MJO time series where daily RMM values are plotted with small dots. The beginning of the time series is indicated by the text alongside the weak amplitude point within the unit circle. The gray X indicates event initiation. MJO termination is noted by the red X. Blue and green dots indicate the start of continuing events, each propagating at least four phases from the start of a continuing event. (b) Same as (a), but for 5 May 1986 – 14 July 1986. A circumnavigating event is highlighted in gold in (b).

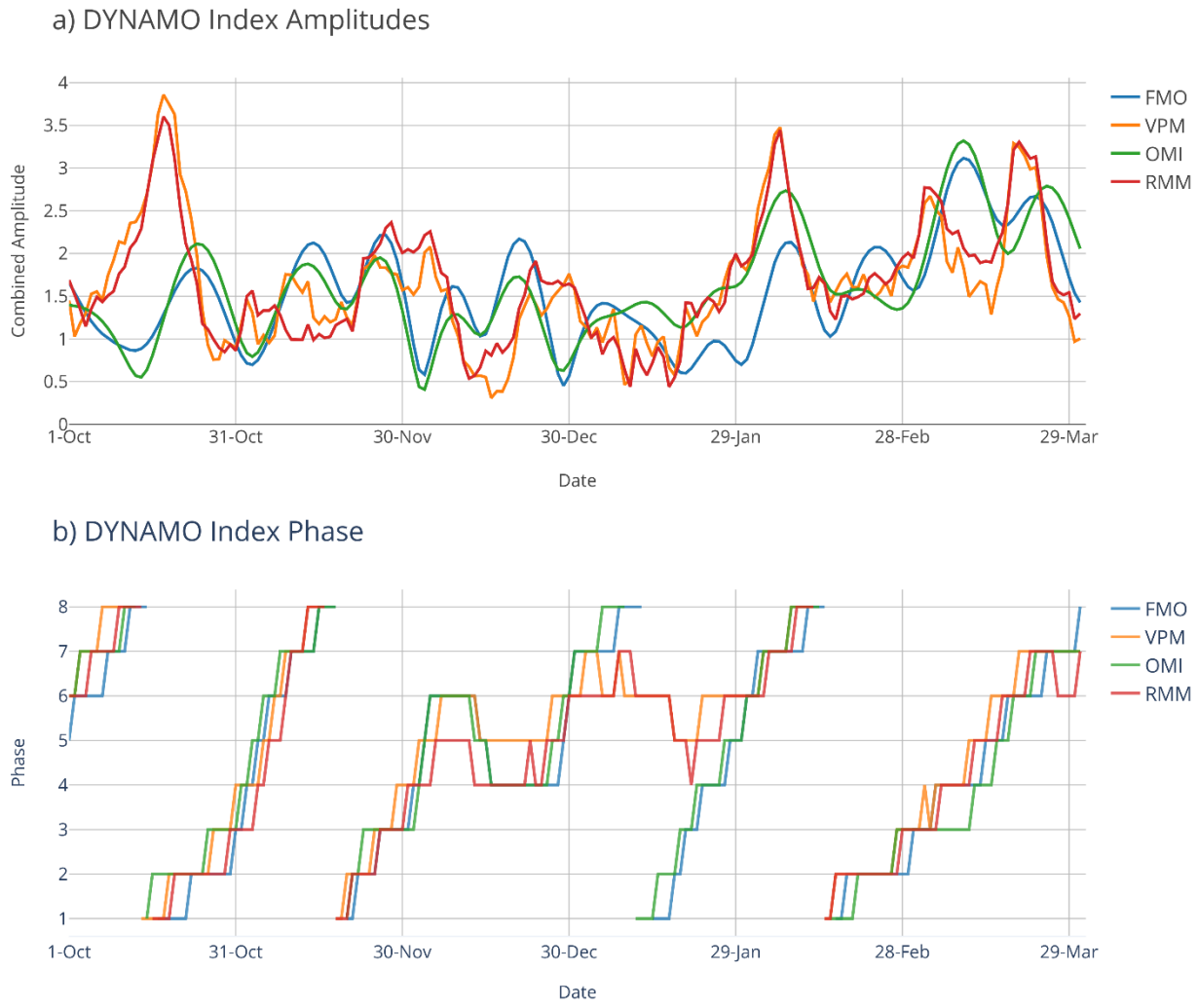

FIG 2.5. Time series of MJO a) daily average combined amplitude and b) phase during the DYNAMO campaign (2011-2012) for the RMM (red), VPM (orange), OMI (green), and FMO (blue) indices.

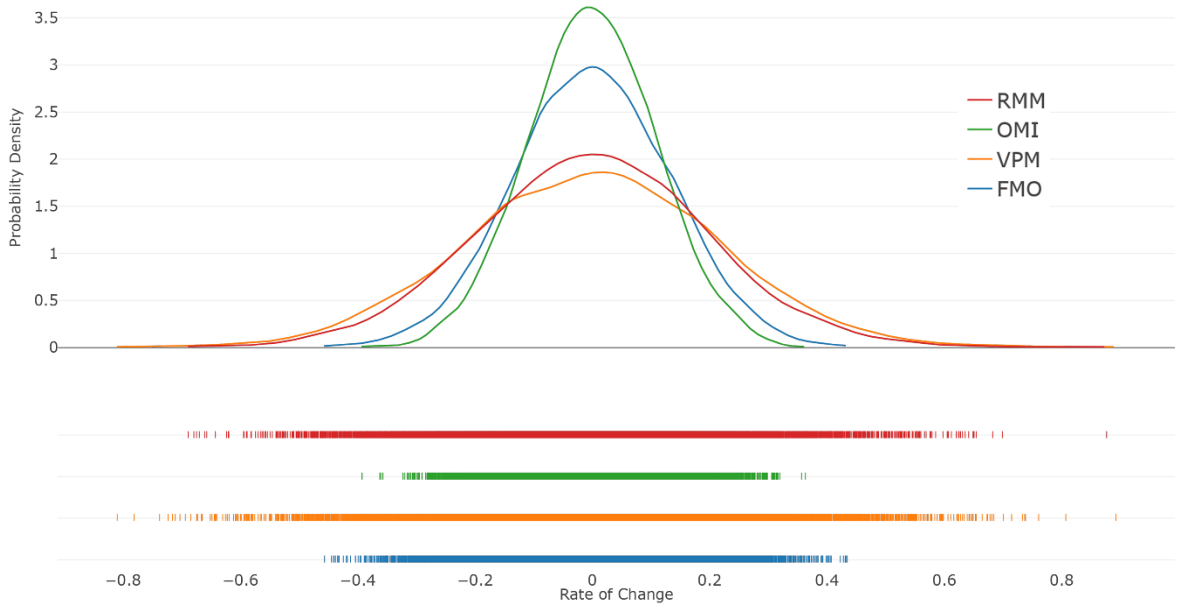

FIG 2.6. Probability density distribution of the daily rate of change in combined amplitude for each index over the 34-year climatology. Horizontal bars below the curves indicate the spread of individual data points throughout the entire period. Data is binned in five hundredth increments.

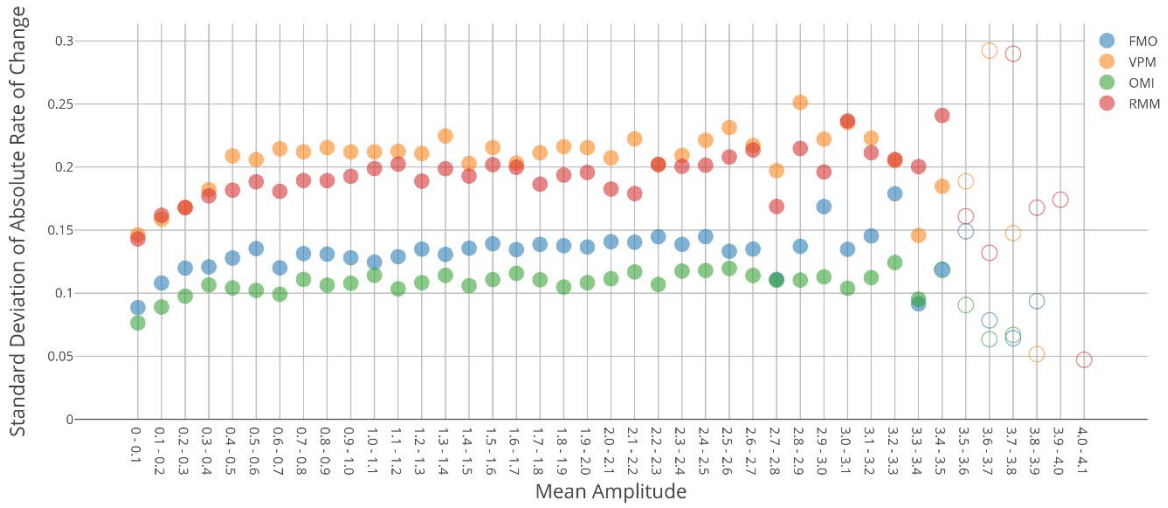

FIG 2.7. Standard deviation of the absolute rate of change as a function of mean amplitude. The mean amplitude is binned every tenth. Open circles indicate those bins with a corresponding number of days that are < 0.1% of the total.

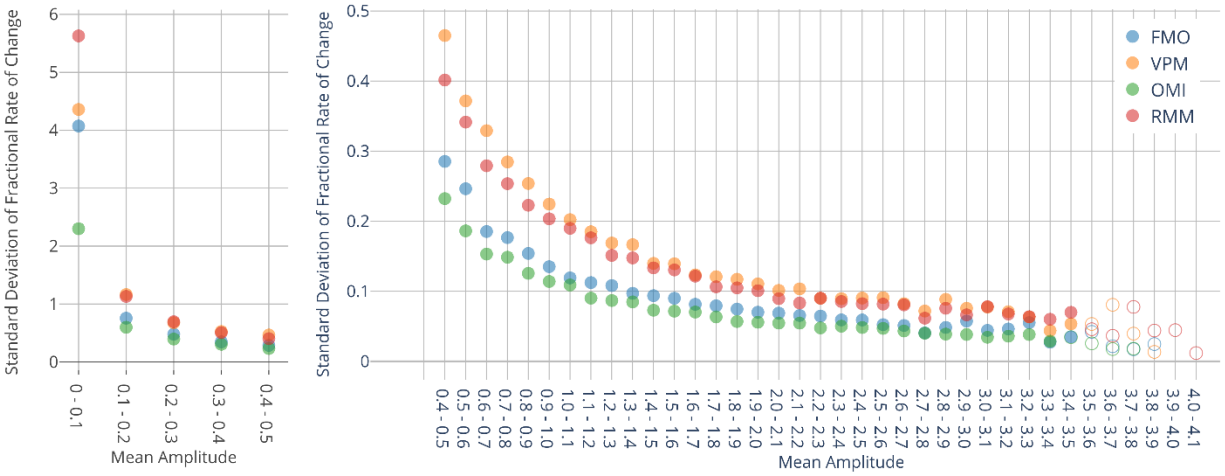

FIG 2.8. Standard deviation of the fractional rate of change as a function of mean amplitude. The mean amplitude is binned every tenth. Open circles indicate those bins with a corresponding number of days that are < 0.1% of the total. Values for 0 to 0.5 are plotted separately (left) so that trends for higher mean amplitude days are more easily identified (right).

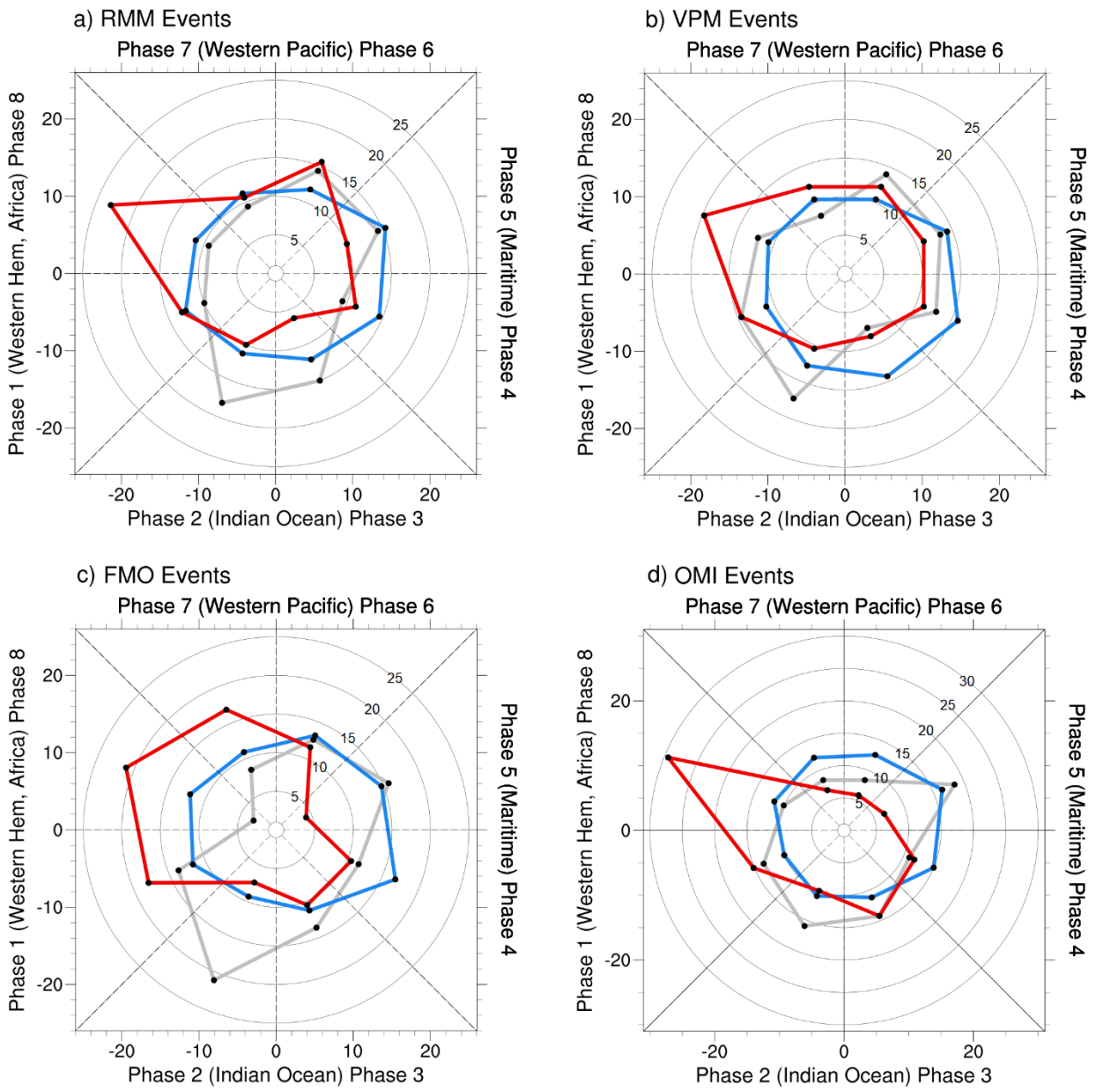

FIG 2.9. Radial-frequency plots of primary, continuing, and terminating events by phase for the a) RMM, b) VPM, c), FMO, and d) OMI. Range rings indicate 1%, 5%, 10%, 15%, 20%, and 25% for panels a) through c). Panel d) has an additional radial rings to account for the higher percentage of terminating events in the OMI where the outer ring indicates 30%.

Chapter III: The Role of Moist Entropy on Termination of Madden-Julian Oscillation Events

3.1 Introduction

The Madden-Julian oscillation (MJO) is the leading mode of intraseasonal variability in the tropics (Madden and Julian 1971, 1972) and has widespread effects on global weather patterns and climate. MJO influences and anomalies include rainfall variability in monsoon regions (Lau and Chan 1986; Matthews 2004; Wheeler and Hendon 2004; Lim et al. 2017), the steering and development of tropical cyclones (Maloney and Hartmann 2000; Jiang et al. 2012; Zhang 2013), and modulations on the El Niño-Southern Oscillation (ENSO, Lau and Waliser 2005; Hendon et al. 2007). Although the MJO teleconnections are many, there is no clear agreement on what mechanisms allow the initiation, maintenance, and termination of the MJO (e.g., Zhang et al. 2013).

The MJO often initiates in the Indian Ocean (IO) region and terminates in the Western Pacific; however, over half of MJO events initiate elsewhere (Matthews 2008). Initiation of the MJO has been widely studied with various mechanisms and environmental conditions investigated for observed and modeled MJOs. These include feedbacks and effects from sea-surface temperatures anomalies (e.g., Wang and Xie 1997; Lau and Shen 1998), air-sea fluxes (e.g., Zhang and McPhaden 2000), moisture and convergence in the planetary boundary layer (e.g., Salby et al. 1994; Wang 1998), radiative feedback from clouds (Raymond 2001; Grabowski 2003), and influences from mid-latitude energy dispersion such as Rossby wave propagation and baroclinic eddies (Zhao et al. 2013) or cold-air outbreaks over the tropics from higher latitudes (Wang et al. 2012).

The active phase of the MJO has amplified convection and precipitation whereas convection is partially suppressed during the inactive phase. The MJO induces a zonal circulation anomaly in the lower- and upper-troposphere (i.e., 850 hPa and 200 hPa, respectively) that most often peaks at wavenumber-1, albeit the coupled convective signal usually varies between zonal wavenumbers 1-3 (Zhang 2005). This envelope of cloud and precipitation anomalies propagates eastward at about 5 m s^{-1}, with individual convective clusters within the MJO propagating to the west (Nakazawa 1988), and demonstrates an intraseasonal cycle of approximately 30 to 90 days. The circulation component of the MJO eventually decouples from the convection over the central Pacific and an increase in propagation speed is observed for the upper-level component of zonal wind anomalies as it potentially circumnavigates the tropics.

Global climate models (GCMs) have historically not performed well with regards to MJO initiation and/or eastward propagation (e.g. Slingo et al. 1996; Kim et al. 2009; Hung et al. 2013; Benedict et al. 2014). Of these, several studies have examined physical mechanisms that may prevent GCMs from accurately simulating the eastward propagation of the MJO. Jiang et al. (2015) used lag-correlations of rainfall over the IO and west Pacific to show only 8 out of 24 GCMs in their study simulated the eastward propagation of the MJO reasonably well. Improved propagation was generally observed when adding air-sea interactions for coupled models. In addition, Jiang et al. (2015) demonstrated that GCMs with poor MJO eastward propagation contained a systematic bias and struggled to simulate a low-level westward tilt with height of diabatic heating and vertical motion, which is often observed in some observations and reanalyses (e.g., Lin et al. 2004; Kiladis et al. 2005; Jiang et al. 2011).

Previous studies have also proposed and focused on the “moisture mode” framework (Yu

and Neelin 1994; Raymond and Fuchs 2009; Sobel and Maloney 2013), where convectively coupled disturbances such as the MJO ultimately have their convection evolution maintained by positive moisture anomalies. Earlier work analyzed intraseasonal moist static energy (MSE) to view the MJO through this moisture mode framework, where MSE anomalies are found to peak in the lower troposphere and predominantly controlled by specific humidity anomalies (e.g., Maloney 2009). More recently, Wang et al. (2017) discovered that an east-west contrast of MSE is crucial for the eastward propagation in GCMs with the contrast observed in scenarios with stronger Rossby waves, poleward meridional wind anomalies, and vertical MSE advection by the second baroclinic mode. Jiang (2017) also used observations and reanalysis to calculate the intraseasonally varying (ISV) moist entropy (ME), a proxy for MSE, and compared vertically integrated ME anomalies and tendency terms for GCMs with either "good" or "poor" eastward MJO propagation. Jiang (2017) found that the MJO Task Force models (Jiang et al. 2015) with enhanced eastward propagation contained a zonal gradient in the ME tendency (i.e., dME/dt) that better matched observations and were largely influenced by horizontal ME advection while simultaneously inhibited by radiative effects and surface heat fluxes. Gonzalez and Jiang (2017) further evaluated MJO performance in GCMs and noted that eastward propagation is handled poorly in models that underestimate mean lower free troposphere (900-650 hPa) moisture over the Maritime Continent (MC), as the mean moisture in the planetary boundary layer (PBL) had little difference among GCMs.

While the majority of studies focus on MJO initiation and maintenance, few studies have investigated the termination and decay of the MJO. A study by Stachnik et al. (2015a) created a climatology of terminating MJO events using methods similar to Matthews (2008) and Straub (2013) and found that termination of the MJO could be a result of its own downstream effect on

the ISV circulation. Specifically, Stachnik et al. (2015a) recognized that intraseasonal vertical circulation anomalies coupled with the mean 850-700 hPa specific humidity best explained the anomalous moisture patterns for MJO events that decayed in several regions. This result contrasts the potential importance of horizontal moisture gradients (e.g., Kerns and Chen 2014) and horizontal ME advection as noted by Jiang (2017). Similar efforts to understand the mechanisms of MJO decay in a low-order dynamical model suggest westward propagating waves may be important for the termination of intraseasonal oscillations (Stachnik et al. 2015b).

Recently, the Stachnik et al. (2015a) termination climatology was expanded in Stachnik and Chrisler (2019) in order to conduct an intercomparison of multiple MJO indices and further test the sensitivity of algorithm parameters used to define MJO events and termination days. Both studies observed a local maximum for terminating events in RMM Phase-8 (western hemisphere) and Phase-6 (Maritime Continent). The western hemisphere maximum is expected since convective anomalies often weaken around the dateline as they decouple from the zonal circulation anomalies associated with the MJO. The second termination maximum over the MC has also been extensively studied with previous work examining the role of disrupting the winds and low-level pressure to the east of the convection (Inness and Slingo 2007), influence of the diurnal cycle (e.g., Hagos et al. 2016), frictional effects and orography (e.g., Inness and Slingo 2007; Tseng et al. 2017), and transient dry precursor signals that weaken propagating moist anomalies (DeMott et al. 2018).

This study follows the work of Jiang (2017) and the moisture mode framework by implementing an analysis of moist entropy (ME) to study termination of the MJO. Rather than focus on GCMs with relatively good or poor climatological MJO eastward propagation, we instead apply similar techniques to analyze differences in the spatial patterns of ME for observed

MJO events that continue through a domain versus those that decay. We furthermore investigate both univariate and multivariate MJO indices to discover any sensitivity of physical conditions associated with MJO termination based on the metrics used. Additionally, we investigate the relative role of ME and its components (including horizontal and vertical advection, surface, and radiative fluxes) for eastward propagation for observed MJO events.

3.2. Data and methods

3.2.1 MJO Indices

This study analyzes both univariate and multivariate indices that are frequently used to track the amplitude and the location of the MJO. The first subset use outgoing longwave radiation (OLR) as a proxy for convection anomalies and include the OLR-based MJO index (OMI) and filtered OLR MJO index (FMO; Kiladis et al. 2014). The OMI index projects 20-96 day filtered OLR onto daily spatial EOF patterns of 30-96 day eastward filtered OLR. The FMO index projects normalized 20-96 day filtered OLR onto a yearly spatial EOF pattern and is averaged between 15°S and 15°N. Aside from the temporal difference of the EOFs (daily for OMI and annual average for FMO), the main difference between these indices is that the OMI EOFs are derived from filtered data that only retains eastward waves whereas the FMO retains all wavenumbers for eastward and westward modes when determining the EOFs.

Common multivariate indices such as the Real-time Multivariate MJO (RMM) index (Wheeler and Hendon 2004) also use upper- and lower-tropospheric (200 hPa and 850 hPa, respectively) zonal wind to track the intraseasonal circulation anomalies in addition to OLR. We also use the Velocity Potential MJO (VPM) index in this study, which is entirely dynamically based and uses a combination of zonal wind anomalies in addition to 200 hPa velocity potential

as a proxy for upper-level divergence and OLR (Ventrice et al. 2013). The RMM and VPM indices are equatorially averaged from 15°S to 15°N, remove the time mean of the climatological cycle and first four harmonics, and use a 120-day running average to subtract longer-term and interannual variations such as variability related to ENSO cycles. Additional details on the MJO indices can be found within the original references.

3.2.2 Defining MJO Events

An event identification algorithm (Stachnik et al. 2015a) is used to define individual MJO events and create a climatology of primary, continuing, and terminating events. Primary events are those that begin from a low amplitude MJO signal and intensify above an amplitude, often unity, that is defined as an active MJO. Continuing events occur from an established MJO signal and terminating events result from the MJO falling below a critical amplitude and/or demonstrating a lack of eastward propagation. The key feature of the algorithm is that it incorporates temporal continuity where a *sequence of dates* is needed to be above some amplitude threshold to define an MJO event rather than compositing by "strong" MJO days with amplitude above a given threshold.

To define eastward propagation and MJO events, the principal components of each index are plotted in a phase-space diagram following Wheeler and Hendon (2004). This MJO strength and location is prescribed by its corresponding location on the phase-space diagram and we require an MJO event to accumulate phase and demonstrate counter-clockwise rotation (i.e., eastward propagation) through at least four oktas (i.e., a half circle) on the phase-space diagram.

Primary events are preceded by a quiescent period or weak MJO signal and later require the MJO to maintain a combined amplitude above a threshold value and propagate through four

phases. The first continuing event requires a minimum of two additional phases beyond a preceding primary event to ensure the signal represents an already established MJO and further accumulates at least four phases. Long-lasting MJO events can therefore contain multiple continuing events as a strong amplitude signal propagates across multiple phase domains. Terminating events are defined when the combined amplitude falls below the active threshold (i.e., amplitude decay) or if the event demonstrates significant westward propagation (i.e., propagation decay). To account for transient weakening or propagation anomalies, the algorithm permits the combined amplitude to drop below unity (but remain above a critical index-specific buffer magnitude) for no more than three days. The MJO is also allowed to temporarily retrograde by a single phase before demonstrating further eastward propagation.

Stachnik et al. (2015a) used a threshold value of unity for defining MJO events and a buffer of one tenth with the RMM index to allow temporarily weakening of the MJO without prematurely terminating an event. Here, we use MJO index specific buffers as determined from a rate-of-change analysis in Stachnik and Chrisler (2019), which permits greater daily amplitude changes (approximately double) for the RMM and VPM indices relative to the OMI and FMO. To examine precursor reasons as to why the MJO might continue or decay, this study focuses on continuing and terminating events and the critical differences with the anomalous ME and associated tendency terms.

3.2.3 Reanalysis Data

Following Jiang (2017), the ERA-Interim reanalysis (Dee et al. 2011) is used in this study. The data includes air temperature and specific humidity that are used to calculate the daily vertically integrated, mass-weighted moist entropy. We also calculate a budget of ME following

Jiang (2017) that includes horizontal and vertical advection, surface fluxes, and net radiative heating, which require zonal and meridional winds, pressure vertical velocity (omega), surface sensible and latent heat fluxes, and shortwave and longwave radiation fluxes at the surface and top of atmosphere from reanalysis. All data is on a 1.5° x 1.5° fixed grid at 32 pressure levels (1000 – 10 hPa), except for the surface and radiative fluxes, and span 34 years (1979-2012) given the availability of overlapping tracking data from all MJO indices. Daily averages for the temperature, specific humidity, and wind data are generated from 6-hourly data. The daily average radiative terms use twice daily (i.e., 00 and 12 UTC), 12-hour forecast average values from reanalysis and are calculated as the difference between the surface and top of atmosphere. Daily average surface flux data are calculated similarly to the radiative terms. Daily anomalies are created for all variables by removing the annual cycle and the first three harmonics. ME anomalies are then time-filtered using a 20-100 day Lanczos filter to create intraseasonal varying (ISV) anomalies.

In the forthcoming discussion, there is a large residual resulting from the ME tendency subterms not summing to zero. This is a known deficiency of reanalysis and consistent with previous work (e.g. Kiranmayi and Maloney 2011; Kim et al. 2014; Jiang 2017). The amplitude of the residual varies among studies and is difficult to compare directly with our results. For example, while primarily using reanalysis, Jiang (2017) used radiative heating estimates from the Hydrologic Cycle and Earth's Radiation Budget algorithm from L'Ecuyer and McGarragh (2010) rather than radiative fluxes from the ERA-Interim reanalysis.

3.2.4 ME Calculation

Previous studies have investigated MJO physics using the moist static energy (MSE)

equation (e.g., Maloney 2009; Kiranmayi and Maloney 2011; Andersen and Kuang 2012; Sobel and Maloney 2012; Kim et al. 2014; Sobel et al. 2014; Pritchard and Bretherton 2014; Inoue and Back 2015; Adames and Kim 2016; Jiang 2017). As convection associated with the MJO is often signaled by moisture anomalies, MSE is appropriate to study the MJO since column-integrated MSE is heavily weighted by contributions from moisture.

We follow the formulations in Jiang (2017), which uses the moist entropy (ME) equation (Raymond et al. 2009; Benedict et al. 2014) as an alternative form of MSE. Specific moist entropy (s) is calculated as

$$s = (C_{PD} + r_v C_{PV}) \ln\left(\frac{T}{T_R}\right) - R_D \ln\left(\frac{p_D}{p_R}\right) - r_v R_v \ln\left(\frac{p_v}{e_{SF}}\right) + \frac{L_v r_v}{T_R} \quad (1)$$

where C_{PD}, R_D, and p_D are the specific heat, gas constant, and partial pressure of dry air respectively; C_{PV}, R_V, p_V, and r_v are the specific heat, gas constant, partial pressure, and mixing ratio of water vapor; T is the air temperature, T_R is the reference temperature of 273.15 K, e_{SF} is the saturation vapor pressure at freezing of 611 Pa, and L_v is the latent heat of condensation at freezing of 2.5×10^6 J kg^{-1}.

Vertically integrated, mass-weighted moist entropy (ME) is written as

$$[\partial ME/\partial t] = \left[\vec{V} \cdot \nabla ME\right] - \left[\omega\left(\frac{\partial ME}{\partial p}\right)\right] + F_s + Q_R \quad (2)$$

where square brackets are mass-weighted integrals from 1000 hPa to 10 hPa, ME is moist entropy where $ME = T_R \cdot s$, $\vec{V}$ is the horizontal wind, ω is vertical pressure velocity, F_S are sensible and latent surface fluxes, and Q_R are shortwave and longwave radiative fluxes. Terms in square brackets are mass-weighted and vertically integrated by applying pressure thickness as weights at each pressure level. It should be noted that the vertical advection of ME is not a conserved quantity and does not only redistribute ME in the column. Here, the vertical advection allows ME to be exported at the top of the column and creates an overturning circulation that

accompanies the upward motion.

Figs. 3.1 and 3.2 show the resulting ME, column-average specific humidity, and column-average temperature for the climatological mean and ISV component, respectively. ME and specific humidity have similar spatial patterns (cf. Figs. 3.1a and 1b, Figs. 3.2a and 3.2b) whereas column-average temperature (Figs. 3.1c and 3.2c) has a weaker horizontal gradient than both ME and specific humidity. While temperature is a factor in ME, the mean and ISV ME is clearly dominated by the specific humidity terms. ME is maximized in the West Pacific warm pool region, deep tropics, and convergence zones, as well as regions with enhanced specific humidity (Fig. 3.1).

3.3 Results for Moist Entropy

3.3.1 Continuing Events

Lead-lag composites of 20-100 day filtered, vertically integrated, mass-weighted, ISV ME anomalies were created for each index for phase-2 (Indian Ocean) and phase-6 (Western Pacific) continuing events. All data are averaged between 10°S and 10°N in the following composites. Each composite has +/- 30 days, where Day 0 for continuing events indicates the first day that the MJO enters a phase domain for an individual event, as identified by each index (see methods).

All indices contain a remarkably similar wavenumber-1 pattern for the continuing phase-2 (Indian Ocean) events (Fig. 3).It should be noted that there is some discontinuity in the composites east of 90°W and near 30°E where interaction with land occurs. Positive ME anomalies are indicative of areas of enhanced convection while negative anomalies are suppressed. The positive anomalies begin at Day -30 for all indices near 90°E and propagate

eastward until reaching the phase-2 domain (i.e., 60-90°E) at Day 0. Amplitude peaks in positive ME anomalies are observed at 90°E between Day 5 and Day 10 and continue to propagate eastward until a break of pattern near or east of the dateline (Fig. 3). Negative ME anomalies also precede and follow the eastward propagating positive anomalies. These negative anomalies peak over a broad region from 120-180°E from Day -10 to Day 0, with a more focused peak from 150-180°E by Day 0. Overall, the ME values are cyclical, consistent with the expectation that MJO events exist before and after Day 0 for continuing events.

MJO events corresponding to the FMO index have the highest magnitude of ME anomalies (Fig. 3d). While there are some magnitude differences for MJO events defined by the different indices, similar ranges (and the same order of magnitude, 10^{-5} J m^{-2}) are identified for all indices. Positive ME anomalies transition to negative anomalies around 90°E at Day 0 for the VPM (Fig. 3b), whereas the zero contour line is slightly more eastward around 120°E for the remaining indices (Figs 3a, 3c, and 3d). It should be noted that the FMO index has less events (n = 24) than all the other indices for phase-2, but nevertheless, contains a similar structure and magnitude to the composite ME anomalies using other indices.

Fig. 4 shows the analogous ME composites for phase-6 (West Pacific) continuing events. A cyclical, wavenumber-1 pattern is again evident for all indices. The first positive anomalies begin at Day -30 slightly east of 60°W for all indices except the VPM, which begins west of 90°W, and propagate eastward with time. These ME anomalies strengthen over the Indian Ocean as the MJO convection couples with the circulation anomaly around Day -20 and eventually peak near Day -10 for the VPM (Fig. 4b) and Day -5 for the other indices (Figs. 4a, 4c, and 4d). The peak positive ME anomalies are centered around 120-150°E for the RMM, OMI, and FMO with a maximum value closer to 90°E for the VPM given its earlier peak. The ME anomalies decrease

in amplitude between dateline and 150°W and the propagation speed of the ISV ME anomalies increases as the MJO convection dissipates over the central Pacific. As in phase-2, negative ME anomalies occur before and after the propagating positive anomalies. Negative anomalies maximize at 90°E around Day 5 for all indices. Generally, there is minimal sensitivity in ME anomaly magnitudes and structures for the various indices for continuing events over the phase-6 domain.

3.3.2. Terminating Events

Figs. 5 and 6 show similar lead-lag composites for MJO termination events for the phase-2 and phase-6 domains, respectively. For these composites, Day 0 refers to the time at which an individual MJO event terminates due to either amplitude or propagation termination (see methods). The number of events (e.g., n = 16 for RMM) is smaller than continuing events (n = 40 for RMM) given that each MJO event can only initiate and terminate once, but long-lasting MJOs will contain multiple continuing events as the MJO propagates into each okta on the corresponding phase-space diagram.

Unlike with continuing events, Fig. 5 shows a clear break in the wavenumber-1 pattern for positive lag days at and after Day 0. Positive anomalies begin at Day -30 around 90°E as with continuing events (cf. Figs. 3 and 4), although the ME anomalies preceding MJO termination propagate eastward in a less coherent manner than for continuing events. The positive ME anomalies end somewhat abruptly at Day 0 around 90°E for termination events identified by the RMM and FMO indices (Figs. 5a and 5d). The VPM and OMI indices meanwhile show slightly more eastward propagation of the positive ME anomalies past Day 0, although the ME anomaly contours are not continuous as with continuing MJO events (Figs. 5b and 5c). Positive ME

anomalies transition to negative anomalies at Day 0 around 110°E for all indices except for the RMM index, which occurs around 130°E. Two minima in negative anomalies occur prior to the termination events, with the first between Day -20 and Day -15 at approximately 90°E and the second occurring around 150°E at or after Day -10 for all indices.

Phase-6 terminating events (Fig. 6) do not have as clear of a break in the wavenumber-1 ME anomaly pattern at Day 0. MJO events using the RMM and VPM index appear to propagate positive ME anomalies farther east (and more continuously) than the other indices (Fig. 6b). Furthermore, the VPM has the lowest amplitude of positive and negative ME anomalies for phase-6. The MJO events using the RMM, OMI, and FMO contain a break in the eastward propagating positive ME anomalies around the dateline near Day -10, whereas the VPM composite first shows a slight break around 100°E before Day -15, 140°E prior to Day -10, and again at 150°W after Day -10. Similar patterns with double maxima in positive anomalies are observed for the RMM, OMI, and FMO (Figs. 6a, 6c, and 6d) at Day -20 at 90°E and Day -10 near 150°E. The FMO has slightly higher amplitudes of ME anomalies for phase-6 terminating MJOs, as was the case with phase-2 (Figs. 5d and 6d). Overall, the terminating events composites are more sensitive to index choice than continuing MJOs, most notably in the positive lag days after the Stachnik et al. (2015a) algorithm identifies a termination event.

3.3.3 Composites of Terminating minus Continuing Events

To observe any significant differences in ME anomalies between event types, composites of the terminal minus continuing MJO event anomalies are created for each index. By design, continuing events always begin on the western edge of a domain and correspond to the first day that the MJO index enters a new phase. To account for potential longitude differences in the

mean location of termination, which can happen several days into a phase domain, we equally subtract three days from the termination composites (i.e., the average propagation into a domain) as a first-order correction before calculating the difference panels. These differences for phase-2 are shown in Fig. 7, where stippling indicates statistically significant different local means using a Student's *t*-test for a 40° averaging window around each point in the longitude-time domain and a test value of 95% ($p = 0.05$).

The following analysis is restricted to patterns that contain statistically significant means between terminating and continuing events. Precursor conditions appear in the multivariate indices (RMM and VPM) starting as early as Day -30 with positive differences occurring west of the IO region (Figs. 7a and 7b). In addition, negative differences (i.e., greater positive ME anomalies for continuing events) occur at Day -10 for the RMM, VPM, and OMI (Figs. 7a-7c) that propagate eastward into the phase-2 domain at Day 0. Furthermore, positive differences (i.e., stronger negative ME anomalies for continuing events) are observed for all indices between 90°E and 120°E starting at Day -10 ahead of the eastward propagating, active region of MJO convection. The presence of statistically significant anomalies in the local domain suggests a different preconditioning of the local environment during the suppressed phase that the MJO eventually enters, consistent with Stachnik et al. (2015a). However, the eastward propagating difference also suggests the strength of the active phase MJO ME anomalies itself may also be a predictor between events that eventually continue or terminate in the phase-2 domain. Differences are observed after Day 0 for all indices, consistent with the notion that the MJO event has appreciably decayed after this time for termination events.

Curiously, westward traveling differences were detected in ISV ME anomalies for the FMO (Fig. 7d). While the other indices contained some suggestion of westward propagating

differences between continuing and terminating events, the RMM, VPM and OMI signals are not as statistically significant. This may result from the lack of additional directional-filtering (i.e., containing westward propagating convectively coupled equatorial waves in the original data) when determining the FMO EOF modes (see Section 2). These waves were not well defined in the spatial patterns of ISV ME anomalies at fixed times before a termination event (discussed later) and their exact cause is a subject of future work and outside the scope of the current study.

Fig. 8 shows the corresponding termination minus continuing event composites for the phase-6 domain. Overall, relatively similar patterns are identified for the OMI and FMO (Figs. 8c and 8d). Negative differences propagate eastward from 90°E to 120°W between Day -10 and Day 10. Likewise, positive differences propagate eastwards from 60°E to 150°W between Day 0 and Day 30, with the FMO having a more consistent propagation of the ME differences between continuing and terminating events. No statistically significant precursor conditions are evident prior to about Day -10 for either of the univariate indices.

Unlike the OMI and FMO, the multivariate indices detect statistically significant different means over the phase-6 domain as early as 30 days prior to a termination event (Figs. 8a and 8b). While the RMM shows the same positive difference at positive lag days in the same region and time as OMI and FMO, the negative ME anomaly difference at positive lag days lasts longer and has a more consistent eastward propagation (Fig. 8a). The previous suggests that zonal wind anomalies have a large effect of the magnitude of the MJO using the RMM index (e.g., Straub 2013) and MJO indices and events incorporating wind metrics are particularly sensitive over domains where the convection typically begins to decouple from the intraseasonal circulation anomalies. Finally, the VPM index has positive differences happening from Day -30 to Day -15 that occur well before the eventual termination event, which also suggest a different long-term

preconditioning of ME in the 30 days prior to the MJO entering the phase-6 domain (Fig. 8b). Negative differences using the VPM also occur from Day -15 to Day 0 between 60°E and 180°E.

3.4. Results for ME Tendency

3.4.1 ME Tendency and Components

The total change in moist entropy was calculated using a centered finite difference by taking the change of ME for every other day throughout the climatology (e.g., Day 3 – Day 1 for Day 2) and expressed as a rate in W m^{-2}. The total ME tendency is further decomposed using the budget in equation (2), which includes horizontal and vertical ME advection, surface heat fluxes, and radiative terms. The surface heat fluxes are separated into latent and sensible fluxes and net column shortwave and longwave radiation for the radiative terms. As in the previous section, composite analysis is used to examine the spatial patterns of total ME tendency and any statistically significant differences between continuing and terminating events.

Although the previous results demonstrated some sensitivity to choice of MJO index, we limit the following analysis to MJO events using the RMM index. Differences in the ME anomaly composites among the various indices were relatively minor for continuing events with a greater sensitivity for termination events. However, the RMM index displayed the greatest difference in ME anomalies after a termination event (i.e., positive lag days) across both domains (Figs. 7a and 8a). Thus, the Day 0 marker best discriminates between a strong and weak MJO signal using this index. Moreover, the RMM is the most commonly used for tracking the MJO, and its subsequent analysis provides a more meaningful comparison with previous work. We first examine differences in the total ME tendency between continuing and terminating events for phase-2 and phase-6 in the following sections in addition to an analysis of the individual

terms comprising the change in ME. Finally, we calculate projection coefficients of each term on the total ME tendency for continuing events (i.e., the favorable pattern for eastward propagation) to observe the relative role of each physical process on the eastward propagation (or lack thereof) of the MJO.

3.4.2 Terminating Minus Continuing ME Tendency Composites

Fig. 9 shows terminating minus continuing composites for 20-100 day filtered, vertically integrated, mass-weighted, anomalous ME tendency (hereafter referred to as tendencies) for RMM Phase-2 and Phase-6, where the patterns discussed are again restricted to those that are statistically significant. In phase-2 (Fig. 9a), negative tendencies begin to appear around Day -25 around the dateline. Additional negative tendency differences (i.e., greater positive tendencies leading up to a continuing event) occur between Day -20 and Day -10 from 10-50°E that propagate eastward (albeit, not continuously) until reaching the IO region at Day 0. Positive tendencies for RMM-Phase 2 events appear around the dateline around Day -15 and reappear east of 120°W a few days later.

Phase-6 (Fig. 9b) has relatively stationary positive tendency differences appearing between Day -30 and Day -25 over the Maritime Continent (MC) and shortly after Day -10 over the IO that propagate eastward up to and after Day 0. Statistically significant negative tendencies appear around Day -15 over the MC, potentially representing a wave train linked to the previous positive tendency differences over this domain. Additional negative tendency differences are observed at Day -5 around 120°W and propagate eastward.

The signs of the total ME tendency leading up to Day 0 in Fig. 9 are different for each phase, which is at first a counterintuitive result. For RMM Phase-2, the positive ME tendency

east of the MC is smaller in magnitude for Day 0 terminating (Fig. 10b) than continuing (Fig. 10a) events. The corresponding negative anomalies west of the MC are larger in magnitude for terminating MJOs, indicating the difference between termination and continuing ME anomalies should always be negative (Fig. 9a). Meanwhile, ME tendencies near 0 W m^{-2} are observed over the central and east Pacific for RMM Phase-6 continuing events (Fig. 10c) with negative tendencies over these domains for terminating events (Fig. 10d). The additional negative tendencies east of the active phase MJO (west Pacific) during phase-6 mean the MJO convection is less likely to propagate eastward for terminating events.

Whereas the continuing composite shows some evidence of a west-to-east gradient with ME tendency becoming less negative (more positive) to the east for continuing events, no such gradient is observed at Day 0 for phase-6 termination events. Given that a positive west-to-east gradient in ME tendency helps with the eastward propagation of the MJO (e.g., Jiang 2017), the composites here suggest the MJO is already locked into a decay pattern prior to Day 0 for events that weaken over the west Pacific. Earlier times thus need to be investigated for bifurcations in the tendency terms and underlying physical processes responsible for termination over the RMM Phase-6 domain. Given these complications, we therefore limit our analysis to the RMM Phase-2 (i.e., IO) as done in Jiang (2017).

3.4.3 Continuing RMM Phase-2 Events

The spatial pattern of anomalous total ME tendency (Fig. 11a) has negative values over Africa and the equatorial western Indian Ocean (IO) with positive values to the east at Day 0 for continuing events. Horizontal advection (Fig. 11e) has both positive and negative tendencies that are spatially like the total ME tendency with a slight eastward displacement and higher in

amplitude (note the range of values vary for some panels in Fig. 11). The vertical advection (Fig. 11c) pattern is more eastward displaced from the total ME tendency and has negative values over the equatorial IO and the MC. The ME tendency from shortwave radiation (Fig. 11d) has the highest amplitude of all terms with negative values maximizing over the equatorial IO and positive values to the east like the vertical advection tendency (Fig. 11d). Longwave radiation (Fig. 11f) tendencies largely mirror the shortwave fluxes and are positive over the western and central equatorial IO with negative values to the east over the MC. Negative tendencies in shortwave radiation indicate the active phase of the MJO where clouds and convection are present, while positive tendencies to the east would suggest the suppressed phase of the MJO. The opposite is true for the longwave heating term. The sensible heat flux (Fig. 11b) has its highest values over land; however, there is a low amplitude, positive anomaly over the IO. The latent heat flux (Fig. 11g) has minimal positive tendencies over the IO with negative tendencies off the east coast of Africa and over the MC region. However, similar maps of latent heat flux for RMM Phase-3 continuing events have positive tendencies over the IO, which is consistent with previous studies examining MJO heating in the IO region (not shown). Finally, the residual (Fig. 11h) has positive tendencies located over the equatorial IO with negative tendencies to the east.

The previous results for observed, continuing MJOs is mostly consistent with the results for GCMs with "good" MJO eastward propagation in Jiang (2017). For example, Jiang (2017) found that horizontal advection projected strongly onto the total ME tendency for good GCMs over the eastern IO and MC and was thus important for the eastward propagation of the MJO. Likewise, the negative values of vertical advection over the eastern IO and MC in Jiang (2017) were determined to be a process that inhibits eastward motion, as is suggested for our observational results. Our primary difference is in the magnitude of the radiative forcing terms,

where we find shortwave radiation to have a larger contribution to the total ME tendency than longwave effects. Jiang (2017) did not use the radiative fluxes from the ERA-Interim data, however, and we thus attribute differences in the total ME tendency to the different data products used in this study.

3.4.4 Terminating RMM Phase-2 Events

The anomalous ME tendency and budget terms for RMM Phase-2 terminating events are shown in Fig. 12, where each panel is shown at ten days prior to the eventual termination (Day -10). We show Day -10 as the MJO has already terminated (e.g., Fig. 10b) by Day 0 and our focus is on the processes potentially responsible for initiating MJO decay.

The total ME tendency (Fig. 12a) has a small area of negative values along the equator off the east coast of Africa with dominant positive tendencies located off-equator over the IO. Positive off-equator horizontal advection tendencies (Fig. 12e) over the IO are somewhat similar to the total ME tendency (Fig. 12a). There is a broad region of sporadic negative vertical advection tendencies over the IO with positive values east over the MC (Fig. 12c). The shortwave radiation fluxes show lower amplitude negative tendencies than for continuing events over the equatorial IO with a strong region of positive ME tendencies east of the MC (Fig. 12d). Longwave radiation tendencies are positive and negative over the equatorial and off-equator IO regions, respectively, with negative ME tendencies prominent over the MC (Fig. 12f). Similar to continuing events, there is a low amplitude positive anomaly over the equatorial IO for sensible heat flux (Fig. 12b), which likely only plays a minimal role in the eastward propagation (or lack thereof) for the MJO. Negative latent heat flux tendencies (Fig. 12g) are located over western IO and positive in central and eastern IO primarily south of the equator. The residual tendencies (Fig. 12h) show a zonal band of positive anomalies over the equator and negative values south of

the equator in the IO region with a broad region of negative ME tendencies east of the MC.

In summary, the Day 0 continuing and Day -10 termination event composites have spatial patterns that are relatively similar with generally lower amplitudes for termination events with the exception of latent heat fluxes (cf. Figs. 11g and 12g). This may indicate that the ISV anomalous ME tendencies have already been locked in prior to Day -10 for future terminating events. The previous result may also explain why the spatial distribution of ME budget terms for termination composites at Day -5 and Day 0 have minimal signs of an active MJO (not shown).

3.4.5. Relative Roles of ME Budget Terms

The relative roles of each ME component in equation (2) are calculated for RMM Phase-2 events. This is done by following Jiang (2017), where the spatial pattern of each ME component over the IO region (10°S-10°N, 50-110°E) are projected for terminating and continuing events, here in daily increments from Day -30 to Day 0. All terms, including the anomalous total ME tendency for termination events, are projected onto the anomalous total ME tendency for continuing events for RMM phase-2 MJOs. Specifically, we aim to determine how the physical processes associated with ME generation or erosion for terminating events differs from continuing events that are associated with the further propagation and maintenance of the MJO. Positive projection coefficients are indicative of the component's contribution for positive ME tendencies to the east of the MJO center, which would favor eastward propagation. The opposite is true for negative projection coefficients, which favor westward propagation. Values close to zero indicate little to no relative role for MJO propagation.

Fig. 13 displays the corresponding projection coefficients for the total ME tendency and individual components to better elucidate when the termination tendencies deviate significantly

from continuing events. Fig. 13a shows the coefficients for the terminating total ME projected onto the total continuing ME pattern for Day -30 to Day 0 in daily increments. Not shown in Fig 13a is the continuing tendency projected upon itself, which results in a value of one. The positive (eastward) projection drops steadily throughout the time series, most notably from Day -25 to Day -20 where the prior amplitude was around 1.0, precipitously decays in magnitude by Day-5, and eventually becomes negative (westward propagation) before Day 0.

Given the previous results, we can examine the individual term projections for deviations between the continuing and terminating composites to help identify those processes responsible for ME differences and potential MJO decay. Fig. 13b shows that horizontal advection tendencies lead towards eastward propagation throughout the entire time series for continuing events, while terminating events still display positive projection coefficients (although often less than for continuing events) through Day -15. There is a significant falloff in the relative role of horizontal advection for eastward propagation in the termination events after Day -15 with a projection coefficient near zero by Day -10 and negative thereafter, consistent with Figs. 11 and 12. The vertical advection tendencies (Fig. 13c) tend to oppose eastward propagation throughout except on Day -15 to Day -10 where continuing events have positive projection coefficients. The corresponding termination composites are negative throughout this entire period.

Shortwave radiation (Fig. 13d) has an exceptionally high amplitude for spatial projection coefficients where the relative role is reversed and favors westward propagation for terminating events from Day -15 until Day -5, unlike the positive projection coefficients for continuing events during this time. Here, the strong negative ME tendency projections from shortwave fluxes likely limits further eastward propagation for terminating events. The longwave radiation (Fig. 13e) also shows differences at and before Day -15 with westward propagation being

favored for continuing events from Day -15 until Day 0 and eastward propagation being favored for terminating events from Day -12 through Day 0. Latent heat fluxes (Fig. 13f) often have different roles for continuing and terminating events throughout the entire 30 days prior to an event occurring in the RMM Phase-2 domain except near Day -15 where the spatial projection coefficients are more similar. Fig. 13f again suggests that the fate of the MJO is sealed no later than Day -10 before the eventual termination given the large differences in the relative role of latent heat fluxes between continuing and terminating events. Sensible heat flux tendencies (Fig. 13g) have overall low projection coefficient amplitudes and thus only exert a limited influence on MJO propagation. The residual tendencies favor eastward propagation throughout the entire time series for both continuing and terminal events (Fig. 13h). We note that although the spatial patterns of the residual term do not always align as well with the anomalous total tendency for continuing events (e.g., Figs. 11a and 11h), the relatively large magnitude of the residual term results in projections coefficients that often exceed unity especially for terminating MJOs.

We find that the Day 0 continuing event projection coefficients are consistent with Jiang (2017) where horizontal ME advection favors eastward propagation and vertical ME advection inhibits eastward propagation. Jiang (2017) showed that total radiative heating favored westward propagation and was dominated by longwave radiation. Our results instead show longwave radiative effects have a near zero projection (projection coefficient of -0.10) with shortwave radiation favoring westward propagation (projection coefficient of -0.42) for continuing Day 0 events. The longwave forcing does favor somewhat stronger westward propagation for two weeks before a continuing event, although the projection coefficients for shortwave ME tendencies are usually stronger (and of the opposite sign) during this period. Furthermore, our results differ for sensible and latent heat fluxes that projected near zero, while Jiang (2017) had a

negative projection for the combined flux for the equivalent of Day 0 continuing events. Other differences in the projection coefficients between continuing and terminating events were observed for horizontal and vertical advection and radiative terms.

Fig. 14 shows the terminal minus continuing composites for these anomalous ME tendency terms. We only show one radiative term as they have similar spatial patterns with signs reversed. We here focus on the statistically significant differences across 50-110°E since the projection coefficients are calculated within that domain. These differences appear at Day -10 for horizontal advection (Fig. 14a), near Day -13 for shortwave radiation (Fig. 14b) and vertical advection (Fig. 14c), and at Day -14 for latent heat flux (Fig. 14d), which are consistent with our projection coefficients. These terms suggest vertical advection may be grouped among the first processes to inhibit eastward propagation due to an ME deficit for termination events, eventually leading to MJO decay.

3.5. Summary and Future Work

As MJO convection is regulated by moisture anomalies, the moisture mode framework can be utilized by implementing moist static energy (MSE) and/or moist entropy (ME) to analyze the maintenance and propagation of the MJO. Overall, ME climatological patterns and intraseasonal varying composites are similar to the composites of specific humidity in Stachnik et al. (2015a), which itself is consistent with the expectation that moist entropy (equation 1) is heavily weighted by the moisture terms (Figs. 1 and 2).

For continuing events, the ME composites for phase-2 and phase-6 MJOs display a cyclical wavenumber-1 pattern with little sensitivity to index choice. Terminating events, however, show a clearer break in the wavenumber-1 pattern for ISV ME anomalies with some minor differences in the resulting termination minus continuing composites for univariate and

multivariate MJO indices (Figs. 7 and 8). The terminating minus continuing events displayed distinct eastward propagation of negative ME differences (i.e., greater positive ME anomalies for continuing events) for all indices except the FMO over the phase-2 domain. In addition, a unique result with westward propagating waves found in the FMO Phase-2 composites that was statistically significant, although further investigation is needed to understand the source and impacts of these potential anomalous westward moving waves. Differences in the lead-lag anomalous ME composites were more pronounced among the various MJO indices for phase-6 MJO events, where the convection typically begins to decouple from the zonal wind anomalies in the upper-troposphere. Overall, ME anomalies were consistently highest for FMO and lowest for VPM when considering MJO event termination.

The spatial patterns for RMM Phase-2 continuing events displayed total ME tendencies that were similar to the contributions from horizontal ME advection and shortwave radiation. Other ME components were displaced east of the main west-to-east tendency dipole (e.g., vertical advection), low amplitude over the local domain (e.g., sensible heat flux), or did not display positive tendencies usually seen with a continuing MJO event (e.g., latent heat flux). The Day 0 continuing and Day -10 terminating events ME tendency composites were spatially similar although the termination composites had lower magnitude tendencies and occasional off-equatorial or asymmetric features for terminating events.

Finally, the projection coefficients revealed the importance of horizontal ME advection for RMM Phase-2 continuing events and its relative role for eastward propagation throughout the entire 30 days prior to the MJO entering the phase space domain. Our Day 0 continuing event projection coefficients were consistent with Jiang (2017), with the exception of the importance of shortwave vs. longwave radiation for changes in ME and the projection of fluxes. A direct

comparison of fluxes is difficult as we separated these into sensible and latent counterparts, while Jiang (2017) had negative projection for the combined flux. Statistically significant differences in projection coefficients for continuing and terminating events are observed for horizontal advection at Day -10 and for vertical advection, shortwave radiation, longwave radiation, and latent heat flux closer to Day -15. These results suggest that multiple processes may concurrently halt further eastward propagation and lead to MJO decay over this domain with the general finding that vertical advection differences in ME is consistent with the deficit of lower-tropospheric specific humidity preceding MJO termination events over the Indian Ocean previously identified in Stachnik et al. (2015a).

Pre-existing MJOs can also interact with a variety of tropical waves generated from other tropical convection and/or waves shed from diurnal forcing over continental domains. Future work will examine how convectively coupled equatorial waves (CCEWs) interact with the MJO during the lifetime of the MJO with an emphasis on transient periods of MJO intensification and decay. Understanding the influence of dry and CCEW interactions with the MJO may produce more reliable and accurate representations of MJO events in weather forecast and GCMs. Studying how these mechanisms work in observations, GCMs, and simple mathematical models is planned for the near future to better elucidate the interaction between moist convection, large-scale flows, and tropical waves.

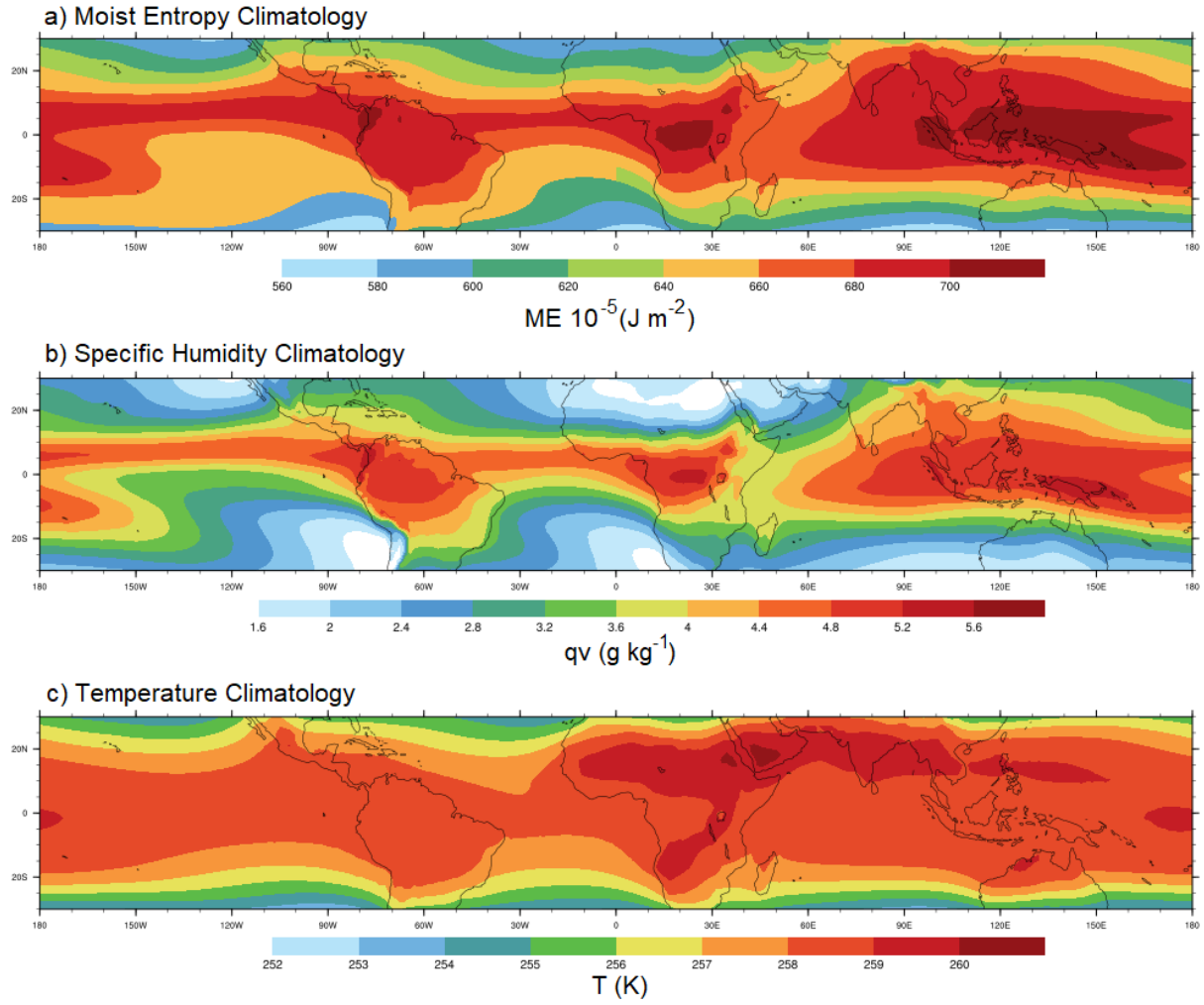

FIG. 3.1. Climatological average of a) vertically integrated, mass-weighted moist entropy, b) vertically averaged, mass-weighted specific humidity, and c) vertically averaged, mass-weighted temperature for 1979-2012.

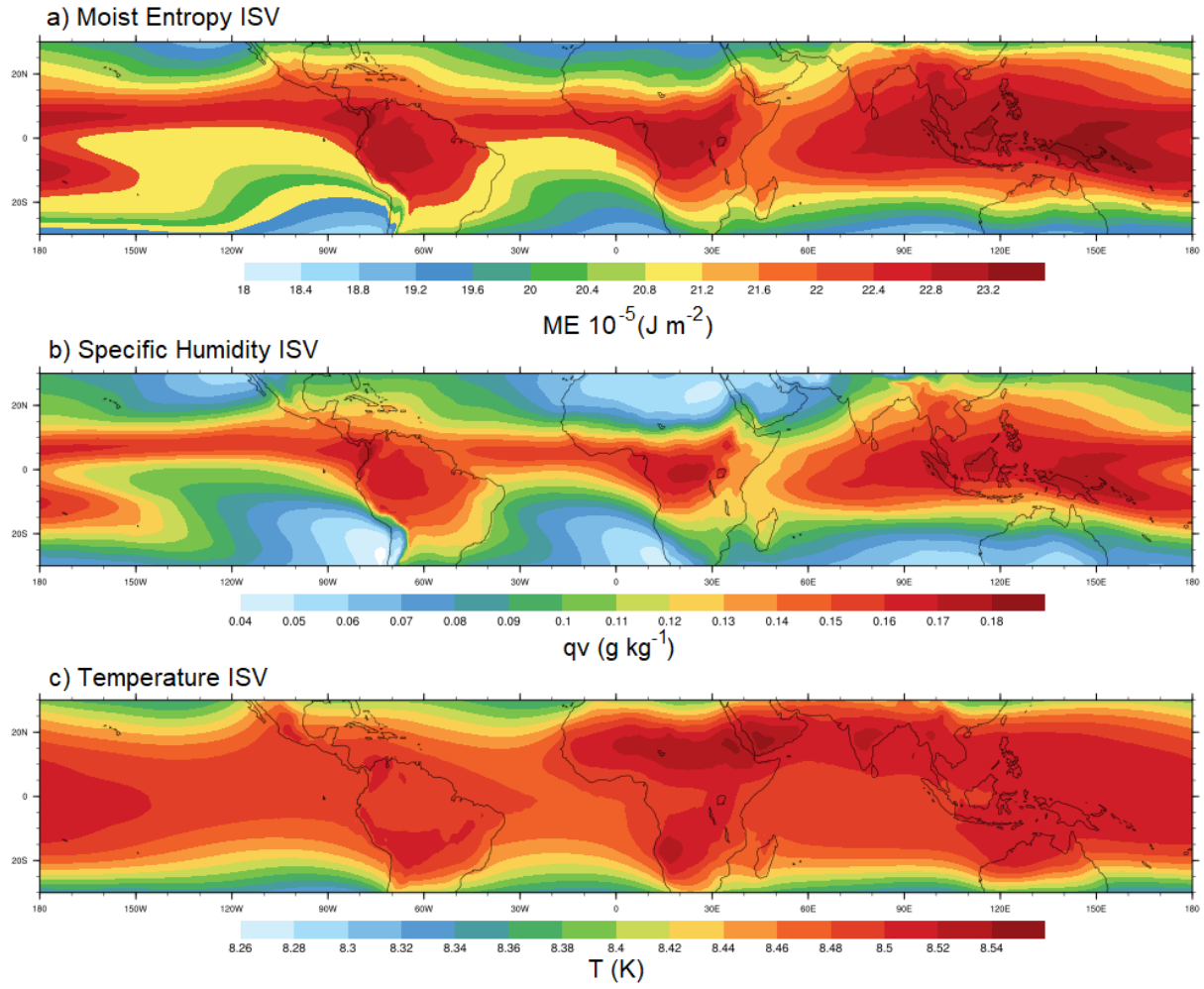

FIG. 3.2. Same as Fig. 3.1, but for the intraseasonally varying (ISV) component of ME.

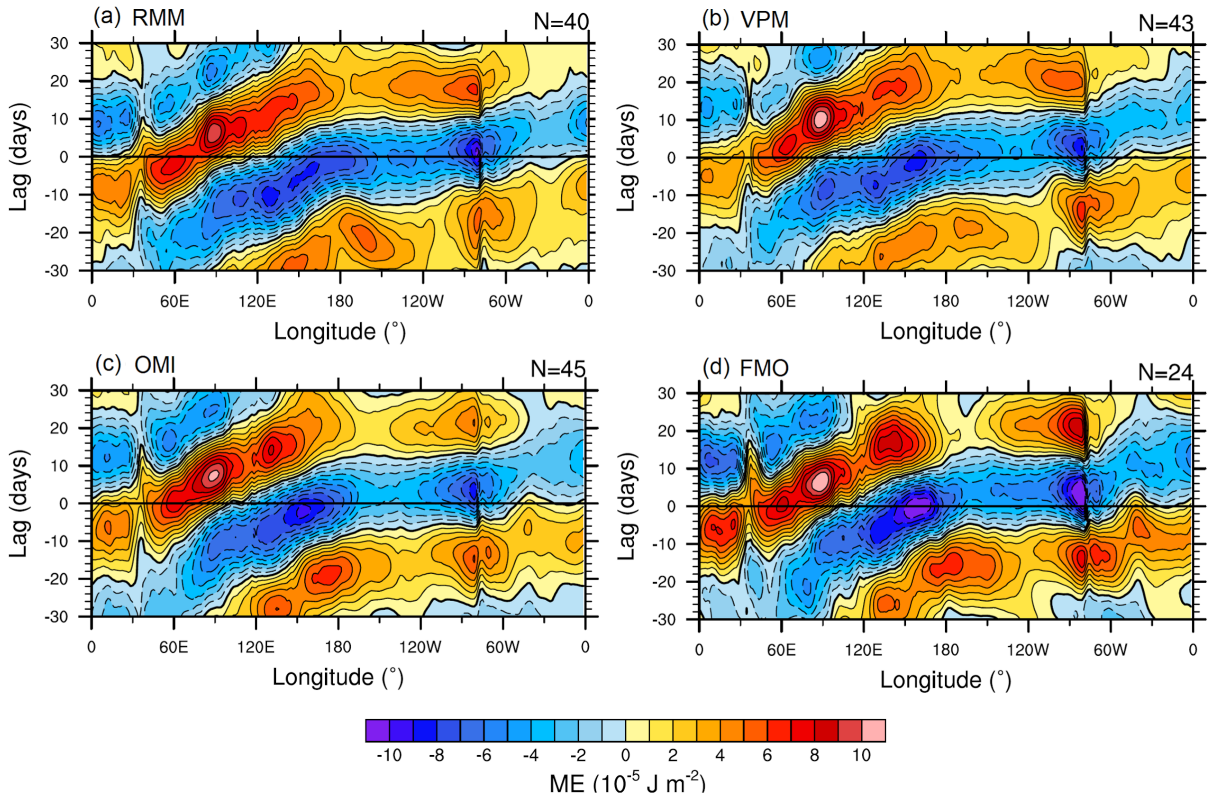

FIG. 3.3. Lead-lag composites of 20-100 day filtered, vertically integrated, mass-weighted moist entropy anomalies from reanalysis for a) RMM, b) VPM, c) OMI, and d) FMO Phase-2 continuing events. All composites are averaged between 10°S and 10°N. The number of events for each composite is represented in upper-right corner of each panel.

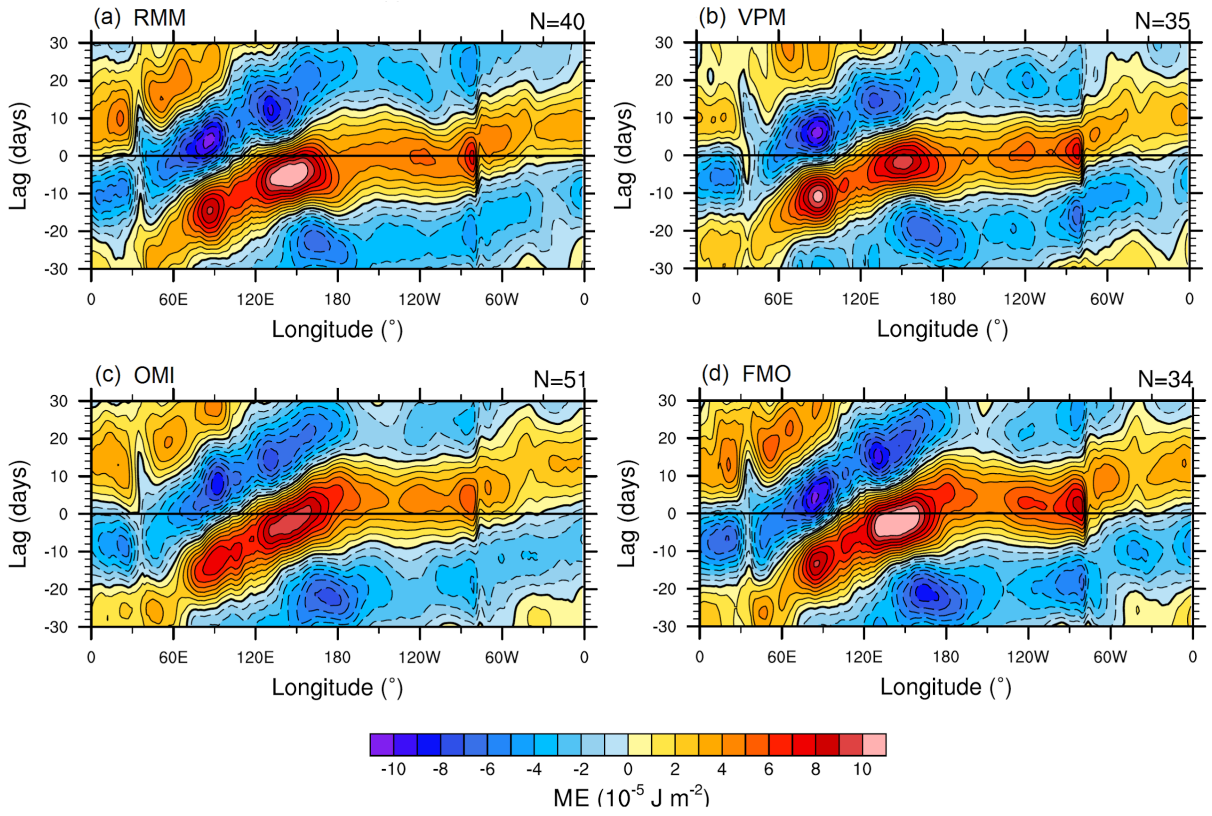

FIG. 3.4. Same as Fig. 3.3, but for phase-6 continuing events.

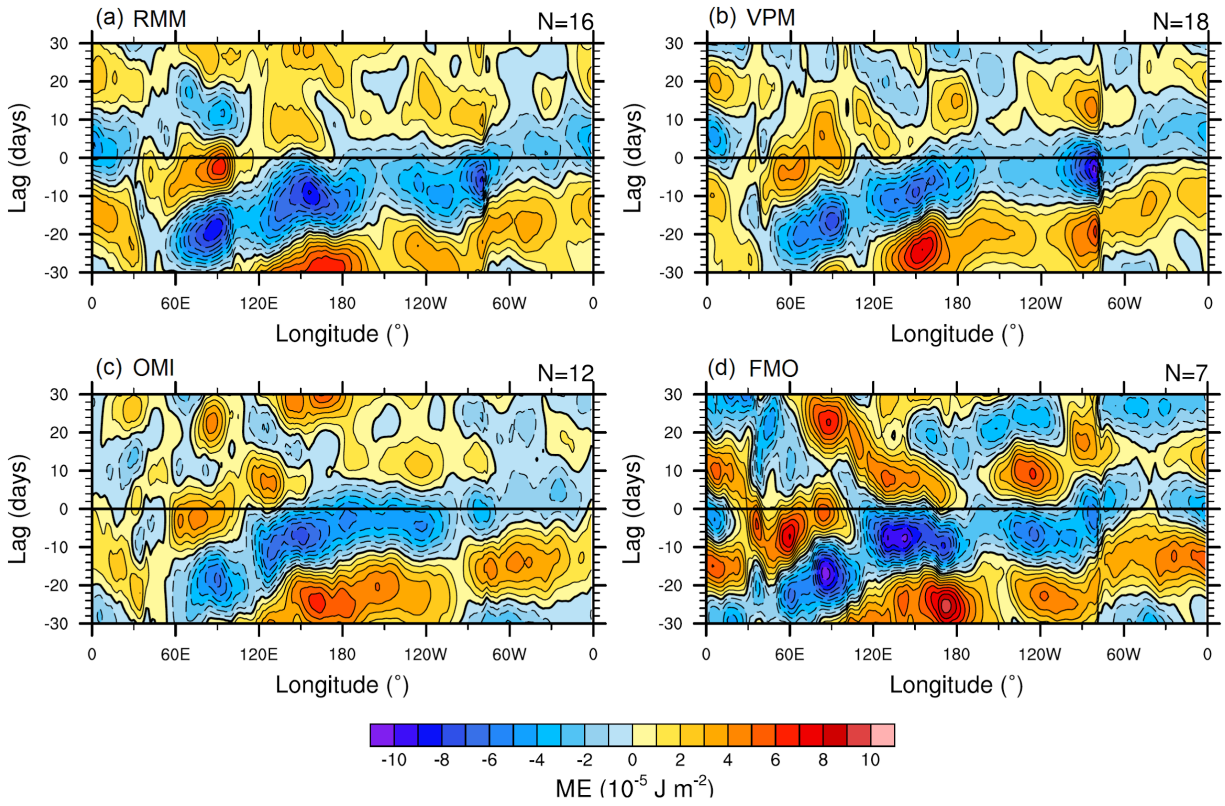

FIG. 3.5. Same as Fig. 3.3, but for phase-2 terminating events.

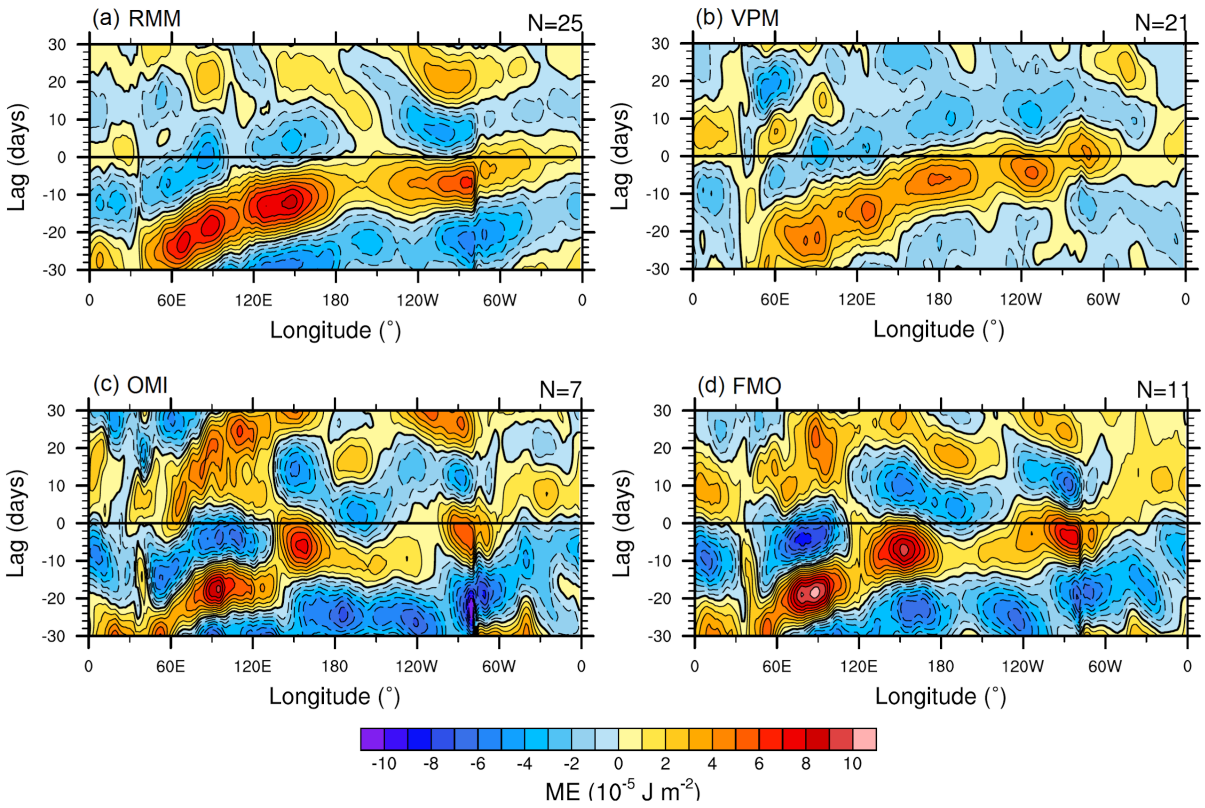

FIG. 3.6. Same as Fig. 3.4, but for phase-6 terminating events.

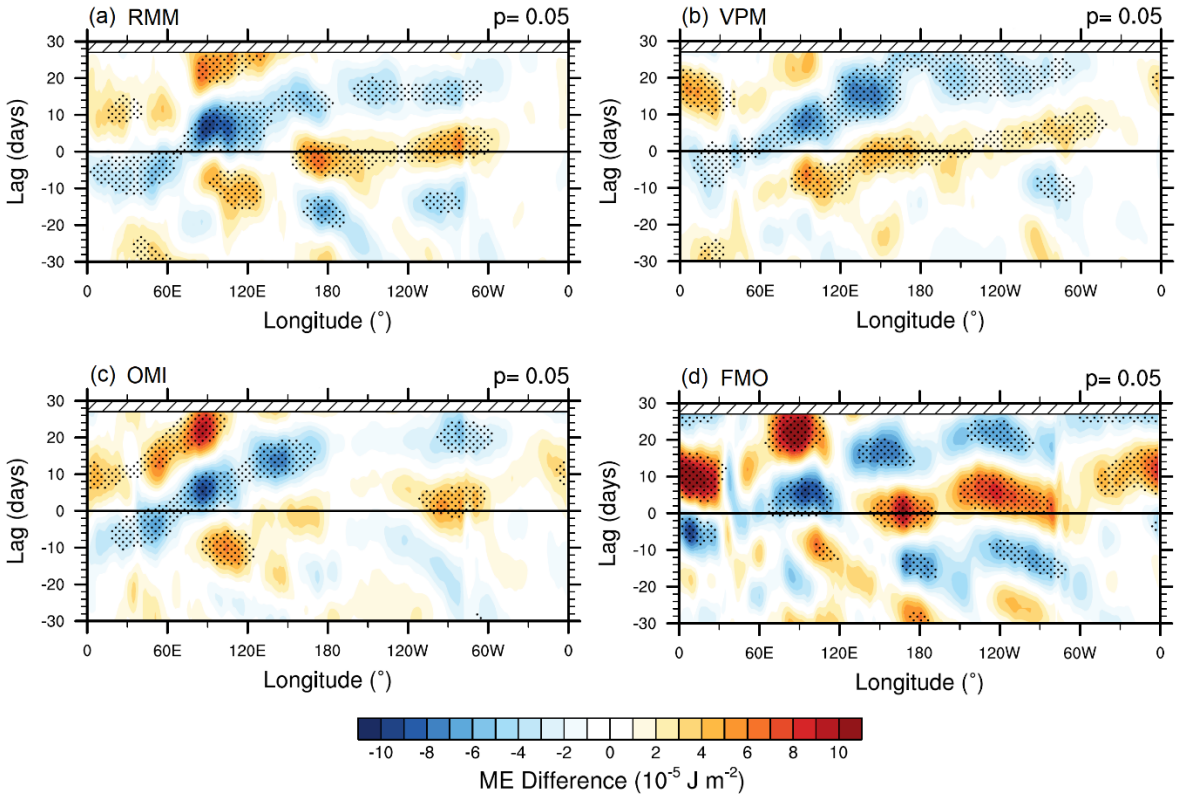

FIG. 3.7. Difference (terminal minus continuing) in 20-100 day filtered vertically integrated, mass-weighted moist entropy for a) RMM, b) VPM, c) OMI, and d) FMO Phase-2 MJO events. Stippling indicates statistically significant local mean for continuing and terminating events using the average of a 40° window centered about the given lag and longitude (see text for further details).

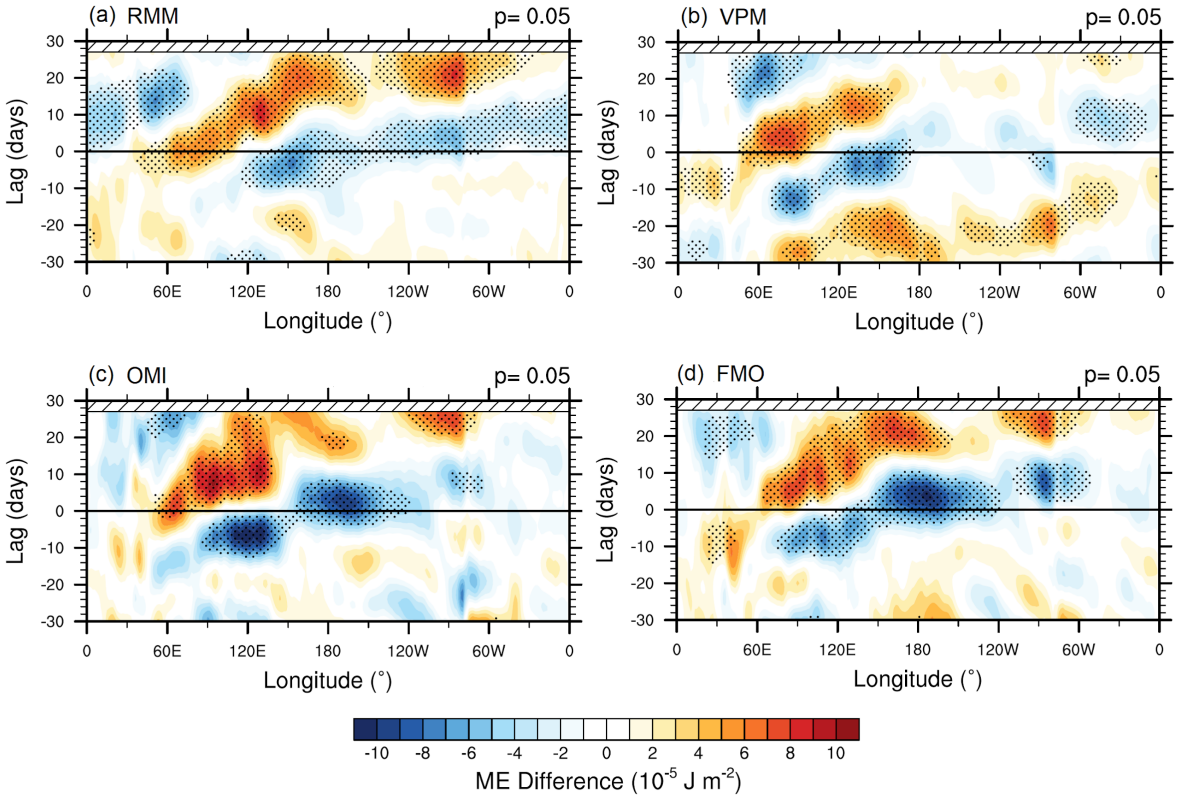

FIG. 3.8. Same as Fig. 3.7, but for phase-6 events.

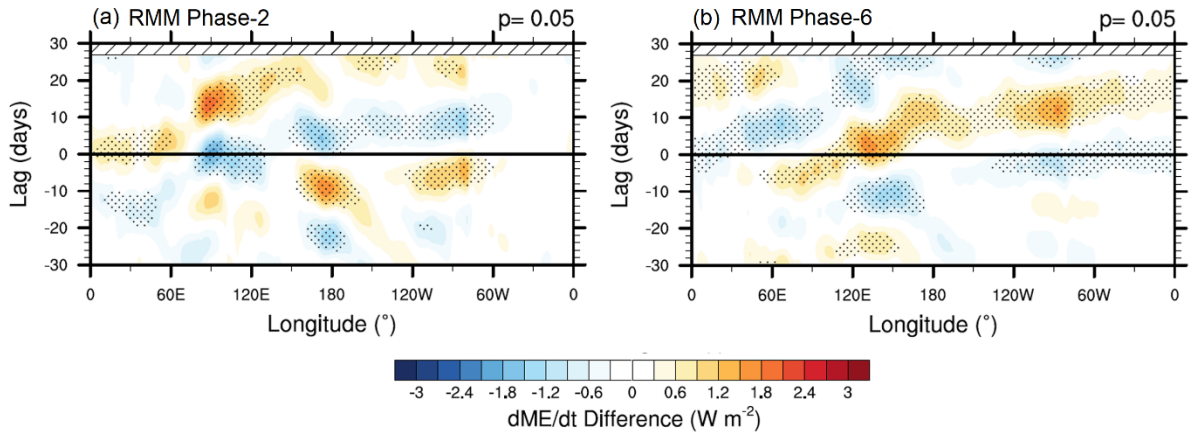

FIG. 3.9. Difference (terminal minus continuing) in 20-100 day filtered, vertically integrated, mass-weighted, anomalous moist entropy tendency for RMM a) Phase-2 and b) Phase-6 domains.

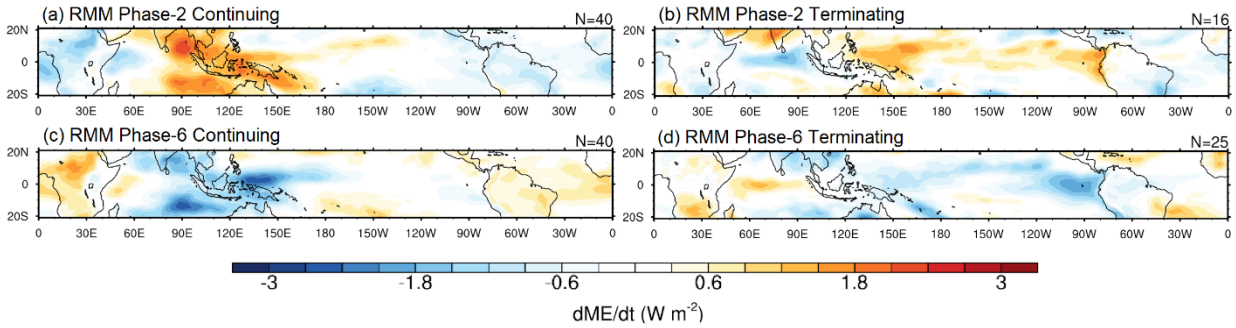

FIG. 3.10. Spatial patterns of 20-100 day filtered anomalous tendencies of ME for RMM Phase-2 a) continuing and b) terminating events. Panels c) and d) are for RMM Phase-6 continuing and terminating events, respectively. All panels are the start of a continuing or termination event (i.e., Day 0).

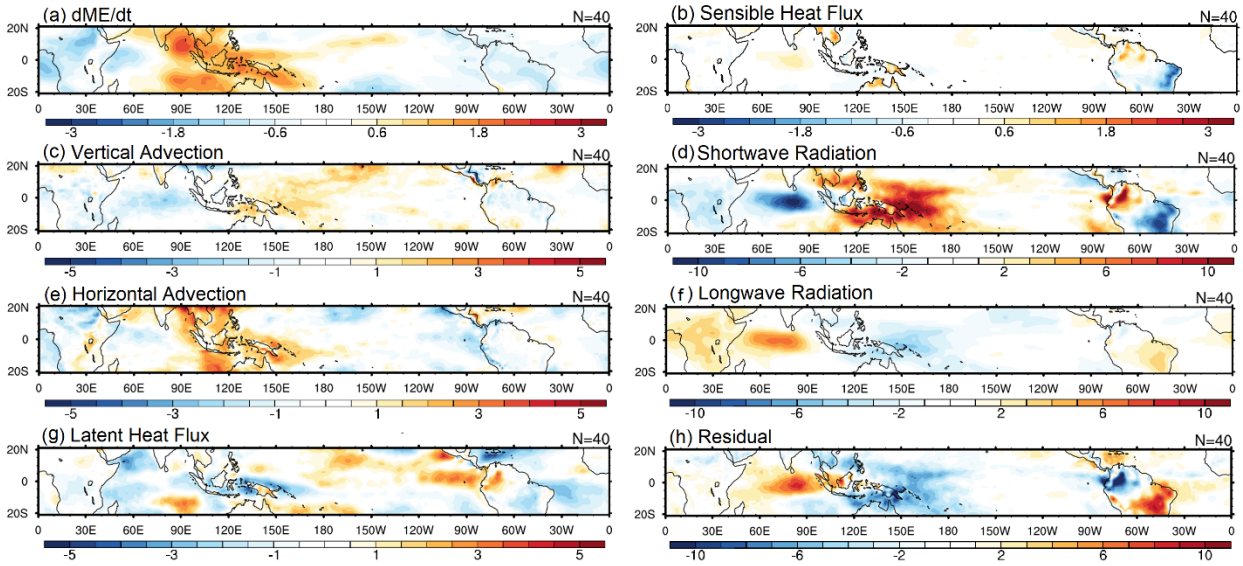

FIG. 3.11. Spatial patterns of 20-100 day filtered anomalous tendencies of a) moist entropy. The total ME tendency is budgeted into contributions from b) sensible heat, c) vertical advection, d) shortwave radiation, e) horizontal advection, f) longwave radiation, g) latent heat flux, and h) residual for RMM Phase-2. Note the magnitude range for the color bar varies among terms. The terms have been ordered so that similar magnitude ranges are grouped together. All panels are for the start of a continuing event (Day 0) and have units of W m^{-2}.

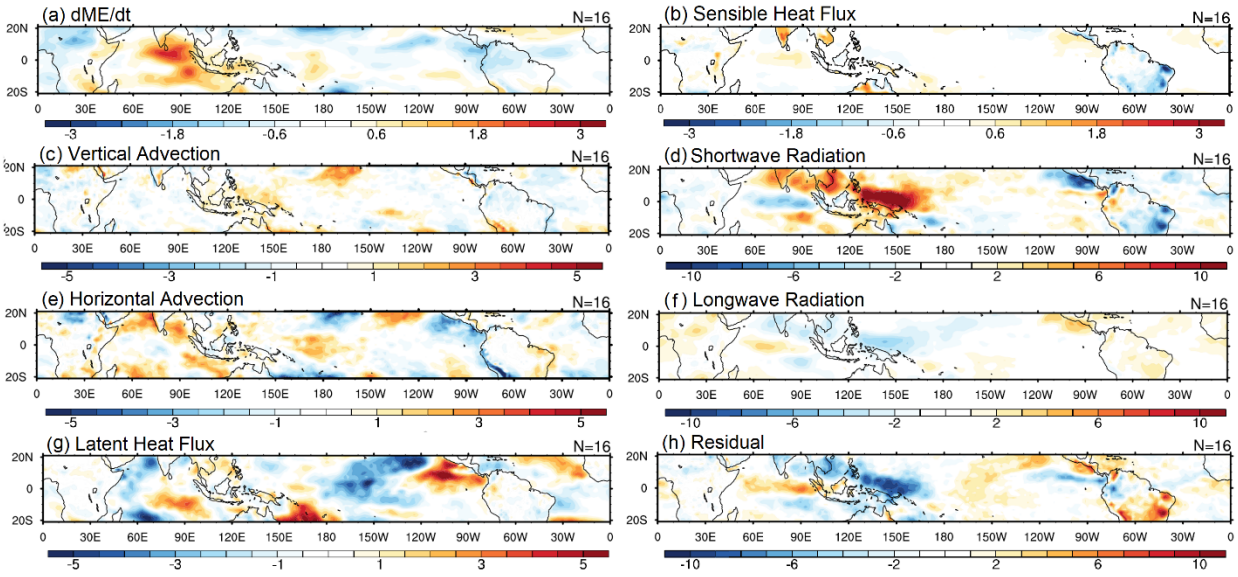

FIG. 3.12. Same as Fig. 3.10, for 10 days prior for a terminating event (Day -10).

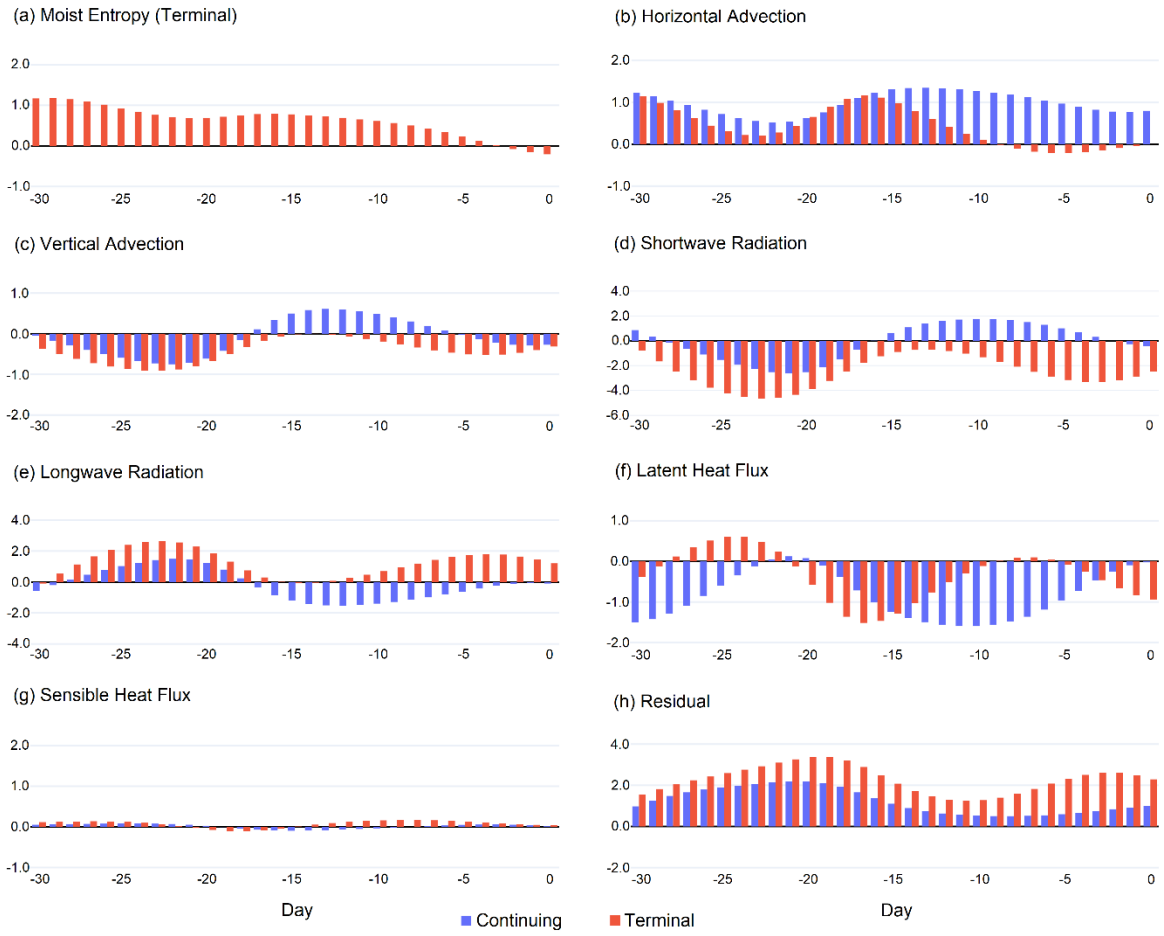

FIG. 3.13 (a) Projection coefficients of the anomalous total ME tendency for terminating events (red) from Day -30 to Day 0 on the anomalous total ME tendency for continuing events. Additional panels show the relative role of b) horizontal advection, c) vertical advection, d) shortwave radiation, e) longwave radiation, f) latent heat flux, and g) sensible heat flux for continuing (blue) and terminating events (red). All projections are on the anomalous total ME tendency for continuing events at the same relative day (e.g., terminating Day -5 and continuing Day -5) over the 50-110°E, 10°S-10°N domain for RMM Phase-2 MJO events. Panel h) includes the projection for the residual from the ISV ME budget.

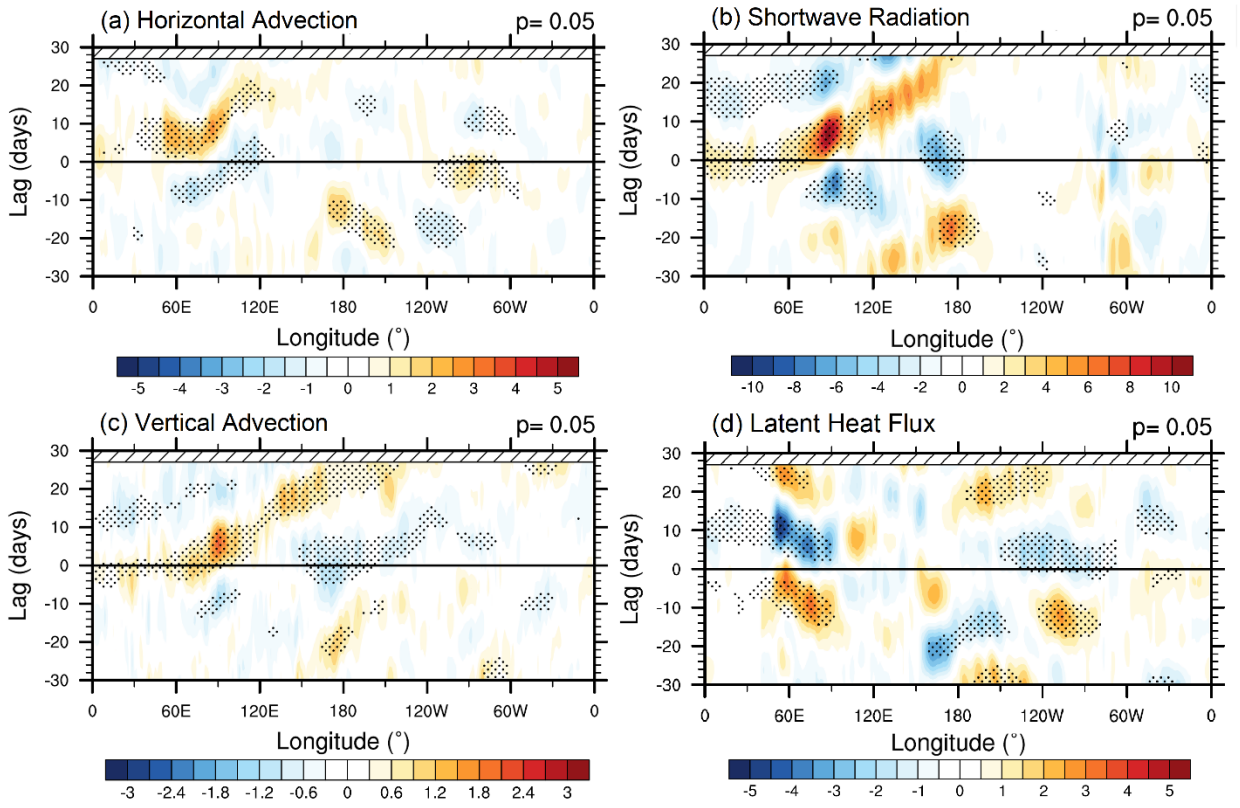

FIG. 3.14. Difference (terminal minus continuing) in 20-100 day filtered a) horizontal ME advection, b) shortwave radiation, c) vertical ME advection, and d) latent heat flux for RMM Phase-2 events. All panels have units of W m^{-2}. Amplitude ranges vary by term and are denoted by the color bar.

Chapter IV: Conclusions and Future Work

The Madden-Julian oscillation (MJO) is the leading mode of intraseasonal variability in the tropics. Although the MJO has significant effects on global climate and weather patterns, it remains poorly represented in global climate models (GCMs). Moreover, the exact reasons behind its initiation, maintenance, termination, and eastward propagation remain an open question and area of in active research. Investigating the sensitivity of indices that track and forecast the MJO may offer insight into physics and dynamics of this climate phenomenon.

There are several indices track the circulation and/or convection anomalies associated with the MJO. A statistical analysis was performed between four common indices where the multivariate indices (RMM and VPM) were susceptible to around twice the daily amplitude rates-of-change than univariate indices (OMI and FMO). Our results suggest that despite differences in metrics used, MJO events terminate most often in the same regions of phase-8 (Western Hemisphere) and phase-1 (Africa) in all indices. There is an exception for the RMM index that has its secondary termination maximum over phase-6 (Maritime Continent), which was consistent with Stachnik et al. (2015a) and is most likely attributed to the MJO struggling to stay convectively coupled after passing through this domain (e.g., Inness and Slingo 2007; Hagos et al 2016, Tseng et al. 2017; Demott et al. 2018). We also determine that multivariate indices are a more reliable metric compared to univariate indices for tracking large-scale MJO termination and decay. This is mainly due to a large frequency of termination events within a single phase for the OMI index and a large inconsistency in the amount of continuing and circumnavigating events between the univariate indices (OMI and FMO).

Recent work has focused on the “moisture mode” framework (e.g. Raymond and Fuchs 2009; Sobel and Maloney 2013; Jiang 2017, Wang et al. 2017) and has noted the importance of

moisture anomalies for regulating the evolution of the convection associated with the MJO. In support of this hypothesis, previous research has investigated specific humidity, gross moist stability, most static entropy (MSE), and moist entropy (ME), among others. These studies noted a west-east gradient of moisture anomalies in observations and models with good simulations of the MJO that assist in the eastward propagation of the MJO (e.g., Jiang 2017). ME, an alternative form of MSE, has been commonly analyzed and deconstructed into advective, radiative, and surface flux components to observe the relative role of each process for the eastward (or lack thereof) propagation of the MJO.

Our analysis of ME shows that there is remarkable agreement for continuing events between the four indices used in the first part of the study for phase-2 and phase-6 MJO events with a cyclical wavenumber-1 pattern evident in all composites. This differs for terminating events that illustrate a clear break in wavenumber-1 pattern. Differences between terminating and continuing composites show eastward propagating, negative ME differences evident of the weaker MJO. We further examine the difference in ME tendencies between terminating and continuing events and note statistically significant different means 25 to 30 days before an ensuing termination event. After breaking the tendency of ME into subterms, we find that horizontal advection provides a significant contribution to the eastward propagation of the MJO for continuing events even up to 30 days prior to entering a phase domain. Furthermore, there are distinct differences in the spatial projection coefficients of ME tendency terms over the Indo-Pacific region between continuing and terminating events for horizontal advection, vertical advection, and radiative terms during the Day –15 and Day –10 timeframe. As several ME tendency terms displayed a large difference (often of opposing sign) in the projection coefficients, multiple processes might be inhibiting the MJO from propagating eastward and

eventually lead to the demise of an MJO event. Our results suggest vertical advection may be the one of the earliest detectable signals for downstream termination of the MJO and is consistent with Stachnik et al. (2015a) who identified a deficit in lower-tropospheric specific humidity in the days prior to terminating events over the Indian Ocean.

Our future work will focus on the influence of convectively coupled equatorial waves (CCEWs) with the MJO with concentration on time periods of transient intensification and weakening rather than simply initiation and/or termination. This will include investigating dry and CCEWs interacting with the MJO in observations, GCMs, and simple mathematical models. Knowledge of how these mechanisms interact may lead toward improved predictions in GCMs and weather forecast models, as well as a better understanding of the interaction between moist convection, large-scale flows, and tropical waves.

References

Adames, Á. F., and D. Kim, 2016: The MJO as a dispersive, convectively coupled moisture wave: Theory and observations. *J. Atmos. Sci.*, **73**, 913–941.

Adames, Á. F., D. Kim, A. H. Sobel, A. D. Genio, and J. Wu, 2017: Characterization of moist processes associated with changes in the propagation of the MJO with increasing CO2. *J. Adv, in Modeling Earth Syst.*, **8**, 2946-2967.

Anyamba, E., E. Williams, J. Susskind, A. Fraser-Smith, and M. Fullekrug, 2000: The manifestation of the Madden-Julian oscillation in global deep convection and in the Schumann resonance intensity. *J. Atmos. Sci,* **57**, 1029-1044.

Andersen, J. A., and Z. Kuang, 2012: Moist static energy budget of MJO-like disturbances in the atmosphere of a zonally symmetric aquaplanet. *J. Clim.*, **25**, 2782–2804.

Bechtold, P., M. Köhler, T. Jung, F. Doblas-Reyes, M. Leutbecher, M. J. Rodwell, F. Vitart, and G. Balsamo, 2008: Advances in simulating atmospheric variability with the ECMWF model: From synoptic to decadal time-scales. *Q. J. Roy. Meteor. Soc.. 134,* 1337–1351, doi: 10.1002/qj.289.

Benedict, J. J., E. D. Maloney, A. H. Sobel, and D. M. W. Frierson, 2014: Gross moist stability and MJO simulation skill in three full-physics GCMs. *J. Atmos. Sci.*, **71**, 3327–3349.

Bond, N. A., and G. A. Vecchi,, 2003: The influence of the Madden-Julian oscillation on precipitation in Oregon and Washington. *Wea. Forecasting*, **18**, 600-613.

Chen, S. S., R. A. Houze Jr., and B. E. Mapes, 1996: Multiscale variability of deep convection in relation to large-scale circulation in TOGA COARE. *J. Atmos. Sci.*, **53**, 1380–1409, https://doi.org/ 10.1175/1520-0469(1996)053,1380:MVODCI.2.0.CO;2.

Dee, D. P., and Coauthors, 2011: The ERA-Interim reanalysis: Configuration and performance of the data assimilation system. *Quart. J. Roy. Meteor. Soc.*, **137**, 553–597, doi:10.1002/qj.828.

DeMott, C. A., B. O. Wolding, E. D. Maloney, and D. A. Randall, 2018: Atmospheric mechanisms for MJO decay over the Maritime Continent. *J. Geophys. Res. Atmos.*, **123**, 5188-5204.

Foltz, G. R., and M. J. McPhaden, 2004: The 30-70 day oscillations in the tropical Atlantic. *Geophys. Res. Lett.*, **31**, L15205, doi:10.1029/2004GL020023.

Gonzalez, A. O., and X. Jiang, 2017: Winter mean lower tropospheric moisture over the Maritime Continent as a climate model diagnostic metric for the propagation of the Madden-Julian oscillation. *Geophys. Res. Lett.,* **44**, p. 2588-2596.

Grabowski, W. W., 2003: MJO-like coherent structure: Sensitivity simulations using the cloud-resolving convection parametrization (CRCP). *J. Atmos. Sci.*, **60**, 847-864.

Guan, B., D. E. Waliser, N. P. Molotch, E. J. Fetzer, and P. J. Neiman, 2012: Does the Madden–Julian oscillation influence wintertime atmospheric rivers and snowpack in the Sierra Nevada? *Mon. Wea. Rev.*, **140**, 325–342.

Hagos, S. M., C. Zhang, Z. Feng, C. D. Burleyson, C. De Mott, B. Kerns, J. J. Benedict, and M. N. Martini, 2016: The impact of the diurnal cycle on the propagation of MJO convection across the Maritime Continent. *J. Adv. Model. Earth Syst.*, **8**, 1552–1564, https://doi.org/10.1002/2016MS000725.

Hall, J. D., A. J. Matthews, and D. J. Karoly, 2001: The modulation of tropical cyclone activity in the Australian region by the Madden-Julian oscillation. *Mon. Wea. Rev.*, **129**, 2970-2982.

Hannah, W. M., and E. D. Maloney, 2011: The role of moisture–convection feedbacks in simulating the Madden–Julian oscillation. *J. Climate*, **24**, 2754–2770

Hendon, H. H., M. C. Wheeler, and C. Zhang, 2007: Seasonal dependence of the MJO-ENSO relationship, *J. Climate*. **20**, 531-543, doi:10.1175/JCLI4003.1.

Higgins, R. W., J.-K. E. Schemm, W. Shi, and A. Leetmaa, 2000: Extreme precipitation events in the western United States related to tropical forcing. *J. Climate*, **13**, 793-820.

Hung, M.-P., J.-L. Lin, W. Wang, D. Kim, T. Shinoda, and S. J. Weaver, 2013: MJO and convective coupled equatorial waves simulated by CMIP5 climate models. *J. Clim*ate, **26**, 6185-6214.

Inness, P. M., and J. M. Slingo, 2007: The interaction of the Madden-Julian oscillation with the Maritime Continent in a GCM. *Quart. J. Roy. Meteor. Soc.*, **132**, 1645-1667.

Inoue, K., and L. Back, 2015: Column-integrated moist static energy budget analysis on various time scales during TOGA COARE. *J. Atmos. Sci.*, **72**, 1856–1871.

Jiang, X., D. E. Waliser, W. S. Olson, W.-K. Tao, T. S. L'Ecuyer, K.-F. Li, Y. L. Yung, S. Shige, S. Lang, and Y. N. Takayabu, 2011: Vertical diabatic heating structure of the MJO: Intercomparison between recent reanalyses and TRMM estimates. *Mon. Wea. Rev.*, **139**, 3208–3223.

Jiang, X. 2017: Key processes for the eastward propagation of the Madden-Julian oscillation based on multimodel simulations. *J. Geophys. Res. Atmos.*, **122**, 755-770.

Jiang, X., and Co-Authors, 2015: Vertical structure and physical processes of the Madden-Julian oscillation: Exploring key model physics in climate simulations. *J. Geophys. Res. Atmos.*, **120**, 4718– 4748.

Jiang, X., M. Zhao, and D. E. Waliser, 2012: Modulation of tropical cyclone activity by the tropical intraseasonal oscillation over the eastern Pacific in a high resolution GCM. *J. Climate*, **25**, 6524–6538.

Kerns, B. W., and S. S. Chen, 2014: Equatorial dry air intrusion and related synoptic variability in MJO initiation during DYNAMO. *Mon. Wea. Rev.*, **142**, 1326–1343, doi:10.1175/MWR-D-13-00159.1.

Kiladis, G. N., J. Dias, K. H. Straub, M. C. Wheeler, S. N. Tulich, K. Kikuchi, K. M. Weickmann, and M. J. Ventrice, 2014: A comparison of OLR- and circulation-based indices for tracking the MJO. *Mon. Wea. Rev.*, **142**, 1697-1715.

Kiladis, G. N., K. H. Straub, and P. T. Haertel, 2005: Zonal and vertical structure of the Madden-Julian oscillation. *J. Atmos. Sci.*, **62**, 2790-2809.

Kim, D., and Coauthors, 2009: Application of MJO Simulation Diagnostics to Climate Models. *J. Climate*, **22**, 6413-6436.

Kim, D., J.-S. Kug, and A. H. Sobel, 2014: Propagating versus nonpropagating Madden–Julian Oscillation events. *J. Climate*, **27**, 111–125.

Kim, H.-M., P. J. Webster, V. E. Toma, and D. Kim, 2014: Predictability and prediction skill of the MJO in two operational forecasting systems. *J. Clim.*, **27**, 5364–5378.

Kiranmayi, L., and E. D. Maloney, 2011: Intraseasonal moist static energy budget in reanalysis data. *J. Geophys. Res.*, **116**, D21117.

Klingaman, N. P., and S. J. Woolnough, 2014a: The role of air–sea coupling in the simulation of the Madden–Julian oscillation in the Hadley Centre model. *Q. J. Roy. Meteor. Soc.*. **140**, 2272–2286, doi:10.1002/qj.2295.

Klingaman, N. P., and S. J. Woolnough, 2014b: Using a case-study approach to improve the Madden–Julian oscillation in the Hadley Centre model. *Q. J. Roy. Meteor. Soc.*, **140**, 2491–2505, doi:10.1002/qj.2314.

Lau, K.-M., and P. H. Chan, 1986: Aspects of the 40–50 day oscillation during the northern summer as inferred from outgoing longwave radiation. *Mon. Wea. Rev.*, **114**, 1354–1367.

Lau, K.-M., and S. Shen, 1998: On the dynamics of intraseasonal oscillations and ENSO. *J. Atmos. Sci.*, **45**, 1781-1797.

Lau, W. K.-M., and D. E. Waliser, 2005: Intraseasonal Variability in the Atmosphere-Ocean Climate System. 2nd ed., p. 613, Springer, Heidelberg, Germany.

Lawrence, D. M., and P. J. Webster, 2002: The boreal summer intraseasonal oscillation: Relationship between northward and eastward movement of convection. *J. Atmos. Sci.,* **59**, 1593-1606.

L'Ecuyer, T. S., and G. McGarragh, 2010: A 10-year climatology of tropical radiative heating and its vertical structure from TRMM observations. *J. Clim.*, **23**, 519–541, doi:10.1175/2009jcli3018.1.

Liebmann, B., G. N. Kiladis, C.S. Vera, A. C. Saulo, and L. M. V. Carvalho, 2004: Subseasonal variation of rainfall in the vicinity of the South American low-level jet stream and comparison to those in the South Atlantic Convergence Zone. *J. Climate*, **17**, 3829-3842.

Lim, Y. L., C. Marzin, P. Xavier, C-P. Chang, and B. Timbal, 2017: Impacts of boreal winter monsoon cold surges and the interaction with MJO on Southeast Asian rainfall. *J. Climate*, **30**, 4267-4281, doi:10.1175/JCLI-D-16-0546.1.

Lin, H., G. Brunet, and J. Derome, 2008: Forecast skill of the Madden–Julian oscillation in two Canadian atmospheric models. *Mon. Wea. Rev.*, **136**, 4130-4149.

Lin, J.-L., M. Zhang, and M. Newman, 2004: Stratiform precipitation, vertical heating profiles, and the Madden–Julian oscillation. *J. Atmos. Sci.*, **61**, 296–309.

Madden, R. A., and P. R. Julian, 1971: Detection of a 40–50 day oscillation in the zonal wind in the tropical Pacific. *J. Atmos. Sci.*, **28**, 702–708.

Madden, R. A., and P. R. Julian, 1972: Description of global-scale circulation cells in the tropics with a 40–50 day period. *J. Atmos. Sci.*, **29**, 1109-1123.

Madden, R. A., and P. R. Julian, 1994: Observations of the 40–50-day tropical oscillation—A review. *Mon. Wea. Rev.*, **122**, 814–837, https://doi.org/ 10.1175/1520-0493(1994)122,0814:OOTDTO.2.0.CO;2.

Maloney, E. D., and D. L. Hartmann, 2000: Modulation of eastern north Pacific hurricanes by the Madden–Julian oscillation, *J. Climate*, **13**, 1451–1460.

Maloney, E. D., 2009: The moist static energy budget of a composite tropical intraseasonal oscillation in a climate model. *J. Climate*, **22**, 711–729.

Matthews, A. J., 2000: Propagation mechanisms for the Madden-Julian oscillation. *Quart. J. Roy. Meteor. Soc.*, **126**, 2637–2651.

Matthews, A. J., 2004: Intraseasonal variability over tropical Africa during northern summer. *J. Climate*, **17**, 2427-2440.

Matthews, A. K., 2008: Primary and successive events in the Madden–Julian oscillation. *Quart. J. Roy. Meteor. Soc.*, **134**, 439–453.

Nakazawa, T., 1988: Tropical super clusters within intraseasonal variations over the western Pacific. *J. Meteor. Soc. Japan*, **66**, 823-836.

Pritchard, M. S., and C. S. Bretherton, 2014: Causal evidence that rotational moisture advection is critical to the superparameterized Madden–Julian oscillation. *J. Atmos. Sci.*, **71**, 800–815.

Raymond, D. J., 2001: A new model of the Madden-Julian oscillation. *J. Atmos. Sci.*, **58**, 2807–2819.

Raymond, D. J., S. Sessions, A. Sobel, and Z. Fuchs, 2009: The mechanics of gross moist stability. *J. Adv. Model. Earth Syst.*, **1**, 20, doi:10.3894/james.2009.1.9.

Raymond, D. J., and Ž. Fuchs, 2009: Moisture modes and the Madden–Julian oscillation. *J. Climate*, **22**, 3031–3046.

Roundy, P. E., C. J. Schreck III, and M. A. Janiga, 2009: Contributions of convectively coupled equatorial Rossby waves and Kelvin waves to the real-time multivariate MJO indices. *Mon. Wea. Rev.,* **470**, 469-478.

Salby, M. L., R. R. Garcia, and H. H. Hendon, 1994: Planetary-scale circulations in the presence of climatological and wave-induced heating. *J. Atmos. Sci*, **51**, 2344 – 2367.

Slingo, J. M., and Coauthors, 1996: Intraseasonal oscillations in 15 atmospheric general circulation models: Results from an AMIP diagnostic subproject. *Climate Dyn.*, **12**, 325–357.

Sobel, A., and E. Maloney, 2012: An idealized semi-empirical framework for modeling the Madden–Julian oscillation. *J. Atmos. Sci.*, **69**, 1691–1705.

Sobel, A., and E. Maloney, 2013: Moisture modes and the eastward propagation of the MJO. *J. Atmos. Sci.*, **70**, 187–192.

Sobel, A., S. Wang, and D. Kim, 2014: Moist static energy budget of the MJO during DYNAMO, *J. Atmos. Sci.*, **71**, 4276–4291.

Stachnik, J. P., and B. Chrisler, 2019: An index intercomparison for MJO event termination. *J. of Geophys. Res. Atmos.*, submitted.

Stachnik, J. P., D. E. Waliser, and A. J. Majda, 2015a: Precursor environmental conditions associated with the termination of Madden-Julian oscillation events. *J. Atmos. Sci.*, **72**, 1908-1931.

Stachnik, J. P., D. E. Waliser, A. J. Majda, S. N. Stechmann, and S. Thual, 2015: Evaluating MJO event initiation and decay in the skeleton model using an RMM-like index. *J. Geophys. Res. Atmos.*, **120**, 11,486–11,508, doi:10.1002/2015JD023916.

Straub, K. H., 2013: MJO initiation in the real-time multivariate MJO index. *J. Climate*, **26**, 1130–1151, doi:10.1175/ JCLI-D-12-00074.1.

Székely, E., D. Giannakis, and A. J. Majda, 2016: Initiation and termination of intraseasonal oscillations in nonlinear Laplacian spectral analysis-based indices, *Math Climate and Wea. Forecasting*, **2**, 1-25.

Tseng, W.-L., H.-H. Hsu, N. Keenlyside, C.-W. J. Chang, B.-J. Tsuang, C.-Y. Tu, and L.-C. Jiang, 2017: Effects of surface orography and land–sea contrast on the Madden–Julian oscillation in the Maritime Continent: A numerical study using ECHAM5-SIT. *J. Climate*, **30**, 9725–9741, https://doi.org/10.1175/JCLI-D-17- 0051.1.

Ventrice M. J., M. C. Wheeler, H. H. Hendon, C. J. Schreck III, C. D. Thorncroft, and G. N. Kiladis, 2013: A modified multivariate Madden-Julian oscillation index using velocity potential. *Mon. Wea. Rev.*, **141**, 4197-4120.

Waliser, D., and Co-Authors, 2009: MJO simulation diagnostics. *J. Climate*, *22*, 3006–3030.

Waliser, D. E., C. Jones, J.-K. E. Schemm, and N. E. Graham, 1999: A statistical extended-range tropical forecast model based on the slow evolution of the Madden–Julian oscillation. *J. Climate*, **12**, 1918-1939.

Waliser, D. E., and M. Moncrieff, 2008: The Year of Tropical Convection (YOTC) Science Plan: A joint WCRP - W WRP/THORPEX International Initiative. WMO/TD No. 1452, WCRP - 130, WWRP/THORPEX - No 9. WMO, Geneva, Switzerland.

Wang, B., 1998: Dynamics of tropical low-frequency waves: An analysis of the moist Kelvin wave. *J. Atmos. Sci.*, **45**, 2051-2065.

Wang, B., and X. Xie, 1997: Coupled modes of the warm pool climate system. Part I: The role of air-sea interaction in maintaining Madden-Julian Oscillation. *J. Climate*, **8**, 2116-2135.

Wang, L., K. Kodera, and W. Chen, 2012: Observed triggering of tropical convection by a cold surge: Implications for MJO initiation. *Quart. J. Roy. Meteor. Soc.*, **138**, 1740-1750, doi:10.1002/qj.1905

Wang, L., T. Li, E. Maloney, and B. Wang, 2017: Fundamental causes of propagating and nonpropagating MJOs in MJOTF/GASS models. *J. of Climate*, **30**, 3743-3769.

Wheeler, M.C., and H. H. Hendon, 2004: An all-season real-time multivariate MJO index: development of an index for monitoring and prediction. *Mon. Wea. Rev.*, **132**, 1917-1932.

Yoneyama, K., C. Zhang, and C. N. Long, 2013: Tracking pulses of the Madden–Julian oscillation. *Bull. Amer. Meteor. Soc.*, **94**, 1871–-891.

Yu, J. Y., and J. D. Neelin, 1994: Modes of tropical variability under convective adjustment and the Madden-Julian oscillation. Part II: Numerical results. *J. Atmos. Sci.*, **51**, 1895–1914.

Zhang, C. D., 2005: Madden-Julian oscillation. *Rev. Geophys.*, **43**, RG2003.

Zhang, C. D., 2013: Madden-Julian oscillation: Bridging weather and climate. *Bull. Amer. Meteor. Soc,.* **94**, 1849-1870, doi:10.1175/BAMS-D-12-00026.1

Zhang, C., and M. Dong, 2004: Seasonality in the Madden-Julian oscillation. *J. Climate.*, **17**, 3169 -3180.

Zhang, C., J. Gottschalck, E. D. Maloney, M. W.Moncrieff, F. Vitart, D. E. Waliser, B. Wang, and M. C. Wheeler, 2013: Cracking the MJO nut. *Geophys. Res. Lett*., **40**, 1223-1230, doi:10.1002/grl.50244

Zhang, C., and M. J. McPhaden, 2000: Intraseasonal surface cooling in the equatorial western Pacific. *J. Climate*, **13**, 2261-2276.

Zhao, C., T. Li, and T. Zhou, 2013: Precursor signals and processes associated with MJO initiation over the tropical Indian Ocean. *J. Climate*, **26**, 291–307, https://doi.org/10.1175/ JCLI-D-12-00113.1.